

Placeholder Title

Master Thesis

C. Christoforidis



PLACEHOLDER TITLE

MASTER THESIS

by

C. Christoforidis

in partial fulfillment of the requirements for the degree of

Master of Science
in Biomedical Engineering

at the Delft University of Technology.

Student number: 4737822
Project duration: 2018 – 2019
Supervisor: Dr. ir. A.L. Schwab, TU Delft
Thesis committee: Dr. ir. R. Happee, TU Delft
MSc. G. Dialynas, TU Delft

This thesis is confidential and cannot be made public until January, 2020.

©2019

C. Christoforidis

ALL RIGHTS RESERVED An electronic version of this thesis is available at
<http://repository.tudelft.nl/>.

ABSTRACT

*C. Christoforidis
Delft, April 2018*

CONTENTS

1	Introduction	1
2	The effect of haptic feedback in the balance task of bicycling	3
2.1	Abstract	3
2.2	Introduction	3
2.3	Methods	4
2.3.1	Description of experimental set-up	4
2.3.2	Description of steer-by-wire controller	4
2.3.3	Experimental Procedure	5
2.3.4	System Identification	5
2.3.5	Comparison Metrics	6
2.4	Results	7
2.5	Discussion and Conclusions	7
3	A gray box analysis on the effect of torque feedback during cycling under lateral perturbations	11
3.1	Introduction	11
3.2	Methods	11
3.2.1	Bicycle Model	12
3.2.2	Rider Control Model	14
3.2.3	Parameter Estimation	15
3.3	Results	16
3.3.1	Zero Delay Model	16
3.3.2	Variable Delay Model	18
3.3.3	Final Model	18
3.4	Discussion	20
3.5	Conclusions	26
A	Calibration of Inertial Measurements	29
B	Orientation Estimation from Inertial Measurements	33
B.1	Offline Estimation Methods	33
B.2	Online Estimation Methods	34
C	Estimation of Rider Torque	39
C.1	Steer rate and acceleration	39
C.2	Steering shaft moment of inertia and viscous friction	39
C.3	Motor Torque Input Validation	42
C.3.1	Design of torque sensor	42
C.3.2	Results	43
Bibliography		47

1

INTRODUCTION

2

THE EFFECT OF HAPTIC FEEDBACK IN THE BALANCE TASK OF BICYCLING

¹Corresponding article: G. Dialynas, C. Christoforidis, R. Happee, A. L. Schwab, The effect of haptic feedback in the balance task of bicycling, In Proceedings of the 4th Triannual International Bicycle and Motorcycle Dynamics Conference (2019).

2.1. ABSTRACT

The objective of this research is to study the effect of haptic steering feedback on the balancing task of a bicycle during lateral perturbation tests, in an effort to improve two-wheeler safety. The steer-by-wire bicycle designed and built at TU Delft bicycle laboratory is used as an experimental platform to analyze the rider response with and without steering feedback. The response of the rider's control actions is represented in the time domain by means of impulse response functions (IRFs). More specifically, three metrics are defined in order to assess both steering and balancing performance. Results failed to indicate any statistically significant difference between experimental conditions. Although, it should be mentioned that parametric rider control identification of the sensory systems might be prerequisite to indicate any possible changes.

2.2. INTRODUCTION

Since the birth of the safety bicycle in the 1890s, dynamics and self-stability have been subjects of numerous discussions and bodies of research. These issues can nowadays be considered to be partly resolved [8] for a wide range of applications. Still, the question remains on how the rider stabilizes the lateral motions of the bicycle when it's driven at low (unstable) forward speeds or how the rider follows a desired path; e.g. the required control inputs and the rider learning process. These probably comprise of haptic, vestibular and visual cues; here we will focus on the haptic cues and the task of stabilization.

Haptic systems in vehicle control are usually connected with two types of realities. One current application of kinesthetic devices is focused on enabling the driver to feel feedback from the vehicle state when steer-by-wire systems come into play. Steer-by-wire vehicles often need a resistance torque to prevent excessive rotation of the steering wheel. This feedback torque is often defined by a simple relation, e.g. a function of wheel angle, wheel torque, or vehicle state, and aims to assist the driver in achieving the desired trajectory in real performance [7]. Similarly, haptics can also be used as a tool to improve first stages of task learning through fading guidance towards a goal [2]. On the other hand, computer simulations can be helpful in evaluating different strategies for steering control [9], as a previous stage to its implementation, and in development of control systems aimed to improve riding safety [10].

In this work we use the experimental steer-by-wire bicycle [5] which has been developed in the TU Delft bicycle laboratory to study the effect of haptic feedback in the balancing task of bicycling. This is achieved by analyzing the rider response with and without steering feedback during lateral perturbation tests. The response of the rider's control actions is represented in time domain by means of impulse response functions

(IRFs). More specific, the applied steer angle and the estimated roll angle is used as a measure of control effort and performance respectively.

The paper is organized as follows: After this brief introduction the experimental set-up and experimental procedure are presented. Next, the methods followed by the results are described. The article ends with the discussion and conclusion section providing further insights in an attempt to explain the findings of this research.

2.3. METHODS

2.3.1. DESCRIPTION OF EXPERIMENTAL SET-UP

At TU Delft an instrumented steer-by-wire bicycle which is fully equipped with a number of sensors to measure the state and rider input has been designed and build, see figure 2.1. For this study measurements from the inertial measurement unit (IMU) sensor (MPU-9250) and the steering angle encoder (RMB-20SC) are used. In addition, a perturbator mechanism is present, which is used to excite the system. These perturbations are applied by laterally pulling a rope with a force transducer in series, which is attached on the seat post. All sensors output are logged with a sampling frequency (F_s) equal to 1000 Hz. The measurement bicycle is electrically driven and has a cruise control system, so the rider does not need to exert pedaling power and thus eliminates the need for lower limb movement. Steering angle (δ) is directly measured from the absolute encoder of the upper front assembly, while the roll angle (ϕ) is estimated from the IMU data using the approach described by Sanjurjo et al. [16].



Figure 2.1: Prototype of the steer-by-wire bicycle with steering and handlebar actuators, sensors, digital controller and custom made battery pack.

2.3.2. DESCRIPTION OF STEER-BY-WIRE CONTROLLER

To minimize the difference between the handlebar angle θ and the fork angle δ , tracking control has been implemented. In this way, the steer-by-wire system should behave like an ordinary, mechanically steered bicycle, when the rider applies a steer torque at the handlebar. Two proportional-differential PD-controllers are implemented in order to provide an action-reaction torque T_{PDH} to the handlebar and T_{PDF} to the fork assembly. Angular velocity $\dot{\theta}$ and $\dot{\delta}$ are estimated by taking the time derivative of angular position θ and δ respectively, for a fixed time interval of 1 ms. The double PD-configuration can also be used to manipulate the steer feedback torque independent of the tracking performance. The double PD-controller is of the following

form:

$$T_{PDF} = K_{PF}(\theta - \delta) + K_{DF}(\dot{\theta} - \dot{\delta}), \quad (2.1)$$

$$T_{PDH} = K_{PH}(\theta - \delta) + K_{DH}(\dot{\theta} - \dot{\delta}) \quad (2.2)$$

with proportional gains K_{PH} , K_{PF} and differential gains K_{DH} , K_{DF} respectively. The torque T_{PDH} is applied at the upper servomotor, and the torque T_{PDF} at the lower servomotor. By setting T_{PDH} to zero a steering configuration is created where the rider feels no reaction torque from the steering assembly (feedback "off"), without majorly affecting tracking error performance. The current controller configuration performs with high level of accuracy up to 3 Hz, the tracking error is kept below 3 degrees. However, in certain conditions non-linear effects of the servomotors and tires might create a delay in the control loop effecting the tracking error and realism of the haptic steering feel.

2.3.3. EXPERIMENTAL PROCEDURE

Twenty healthy subjects volunteered in this study. To assure safety all subjects were requested to wear protective equipment in the shape of a standards-approved bike helmet, knee and elbow pads. All participants gave informed consent according to the guidelines of the human research ethics committee of Delft University of Technology. All subjects were healthy and reported that they did not experience any kind of pain or injury in the year before the experiments. The mean weight of all subjects was selected to be close to the European population [20].

Each experiment trial consisted of four different speeds (i.e., 2.6, 3.7, 4.5, 5.6 m/s). Two individual trials were performed in total for every speed. In the first trial steering feedback was enabled, whereas in the second trial steering feedback was disabled. Every trial had a duration of approximately 60 seconds. All experiments were performed across Heertjeslaan cycling path of TU Delft, the subjects were requested to ride the steer-by-wire bicycle in all aforementioned speeds while being laterally perturbed. An additional bicycle was used from the experiment coordinator to cycle next to the instrumented steer-by-wire bicycle and perturb the subject, see figure 2.2. A set-up which allowed both push and pulls was initially tested but the pushes were subject to inconsistencies. After inspecting the data of the pilot runs, it was observed that unilateral disturbances did not affect the predictability of the perturbation, as the response of the rider was similar. For this reason the unilateral approach was chosen. Nevertheless, to avoid any feedforward control behaviour (e.g., seeing the coordinator preparing to pull the rope) all subjects were asked to keep their focus on the road ahead.

2.3.4. SYSTEM IDENTIFICATION

In order to remove the effects of unwanted disturbances and noise, the measured steering angle and estimated roll angle signals were filtered through a finite impulse response (FIR) model. The impulse response function is defined as the function $h(\tau)$ which when convoluted with external input $w(t)$ results in the output $y(t)$. The output data either represents $y(t) = \phi(t)$ corresponding to $h_\phi(\tau)$ or $y(t) = \delta(t)$ corresponding to $h_\delta(\tau)$. In discrete time the convolution can be approximated by the following equation:

$$y(t) = \sum_{\tau=0}^{T-1} h(\tau) w(t-\tau) \Delta\tau + v(t) \quad (2.3)$$

where T is the time length of the impulse function, which is equal to 3.08 seconds as the oscillations die out after that point and $v(t)$ the remnant which is caused by unwanted disturbances. Equation C.2 is rewritten in matrix form as follows:

$$y = Wh + v \quad (2.4)$$

where W is the matrix containing time shifted versions of the input signal.

$$W = \begin{bmatrix} w(0) & 0 & 0 & \dots & 0 \\ w(1) & w(0) & 0 & \dots & 0 \\ w(2) & w(1) & w(0) & \dots & 0 \\ \vdots & \vdots & \vdots & \ddots & 0 \\ w(N-1) & w(N-2) & w(N-3) & \dots & w(N-T) \end{bmatrix} \quad (2.5)$$



Figure 2.2: Experimental trial performed across Heertjeslaan cycling path of TU Delft; Experiment coordinator cycling next to steer-by-wire bicycle while pulling laterally the subject with a rope.

Since equation 2.4 is linear in the parameters (the coefficients of h) there exists a unique solution that can be found through the least squares method.

$$\hat{h} = (W^T W)^{-1} W^T y \quad (2.6)$$

Having an estimate of the IRE, the input signal is convoluted with (\hat{h}) in order to produce an estimate of the output (\hat{y}) without the noise. The estimated responses are further smoothed using a eight-order Butterworth filter with cutoff frequency of 10 Hz.

2.3.5. COMPARISON METRICS

In order to correctly assess if there is a statistically significant difference between the two conditions, three metrics are defined. The first one is the Power Spectral Centroid (PSC) of measured angle (δ) defined as

$$(PSC_x, PSC_y) = \left(\frac{\sum_{n=1}^N f(n) S_\delta(n)}{\sum_{n=1}^N S_\delta(n)}, \frac{\sum_{n=1}^N S_\delta(n)^2}{\sum_{n=1}^N S_\delta(n)} \right) \quad (2.7)$$

where N is the number of samples lower than 5 Hz and $S_\delta(f)$ the power spectral density of the signal. This metric gives an indication of the frequency which most of the power in the signal is centered around. Higher value of PSC_x will indicate more oscillatory behaviour for the steering response and can be used as a metric of control effort.

The variance accounted for (VAF) is used to assess the quality of the fit of the FIR model output. The runs which scored lower than 60% were removed from further analysis as it was deemed that the model did not sufficiently capture the characteristics of the raw signal. The VAF between \hat{h}_ϕ^{off} and \hat{h}_ϕ^{on} is also used as a metric of similarity for the roll angle response. In that case VAF is defined as :

$$VAF_\phi = \left(1 - \frac{\text{var}(\hat{h}_\phi^{off} - \hat{h}_\phi^{on})}{\text{var}(\hat{h}_\phi^{off})} \right) \cdot 100\% \quad (2.8)$$

Finally as a third test, the relative delay between the steering angle IRFs of the two conditions is estimated by finding the lag value of maximum cross-correlation between the signals.

2.4. RESULTS

An independent 2-sample t-test was conducted to compare if there was significant difference (95 % confidence interval) in steering effort between conditions for all speed levels, see figure 2.3. For the low speed level (2.6 m/s) there was no significant difference in PSC_x for "feedback on" ($M = 0.79$, $SD = 0.08$) and "feedback off" ($M = 0.76$, $SD = 0.10$) conditions; $t(38)=1.00$, $p=0.3222$. For speed 3.7 m/s there was again no significant difference in the metric for "feedback on" ($M = 0.92$, $SD = 0.11$) and "feedback off" ($M = 0.92$, $SD = 0.11$); $t(38) = -1.03$, $p=0.3075$. For 4.5 m/s there was also no significant difference in the scores for "feedback on" ($M = 0.98$, $SD = 0.14$) and "feedback off" ($M = 0.98$, $SD = 0.14$); $t(38) = -1.04$, $p=0.3062$. And finally, for 5.6 m/s no significant difference was found in the PSC_x for "feedback on" ($M = 1.1$, $SD = 0.16$) and "feedback off" ($M = 1.1$, $SD = 0.16$) conditions; $t(38) = -1.6$, $p=0.118$.

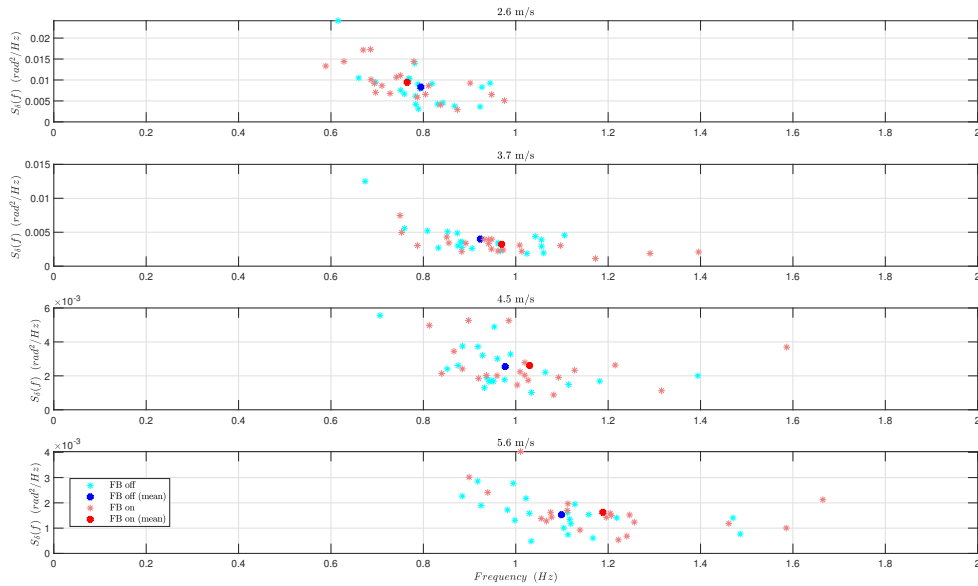


Figure 2.3: The x and y coordinate of the PSC used to determine the frequency where most of the power is concentrated.

The impulse response function of the mean rider for steer angle (δ) and roll angle (ϕ) is shown in figure 2.4. The variance accounted for between roll angle impulse responses (see equation 2.8) is averaged over all participants and displayed for all speed levels in figure 2.5 (a). Similar roll angle response between "feedback on" and off indicated by higher VAF_ϕ values suggests matching task performance.

In addition to the variance roll test an one-sample t-test was conducted to examine if there is any delay in the steering response between feedback on and off, see figure 2.5 (b). For 2.6 m/s there was no significant deviation in the delay ($M = -3$, $SD = 25.89$) from zero mean; $t(19) = -0.52$, $p=0.6103$. However, for 3.7 m/s the delay ($M = -20.65$, $SD = 25.93$) was statistically significant; $t(19) = -3.56$, $p=0.0021$. Also for 4.5 m/s the mean of the delay ($M = -23.5$, $SD = 20.88$) was also significantly different than zero; $t(19) = -5.03$, $p=0.0001$. Lastly, for 5.6 m/s there was again significant difference in the delay ($M = -19.15$, $SD = 18.19$) from zero; $t(19) = -4.71$, $p=0.0002$.

2.5. DISCUSSION AND CONCLUSIONS

From the aforementioned results it is suggested that the effects of haptic feedback are minimal to non-existent for the roll stabilization task. Neither performance (see figure 2.5 (a)) or steering effort was affected by the removal of haptic steering feedback. Balance performance among conditions was comparatively consistent (see figure 2.5 (a)). However, in the unstable speed region the variance and the number of outliers were higher. For steering effort the null hypothesis that the PSC_x metric came from independent random samples with equal means and equal variances failed to be rejected for all speed levels. This does not undoubtedly prove that the samples came from the same population, howbeit it gives a strong indication towards that fact. On the other hand, for the "feedback on" the steering response was delayed (≈ 18 ms see figure 2.5 (b)) in

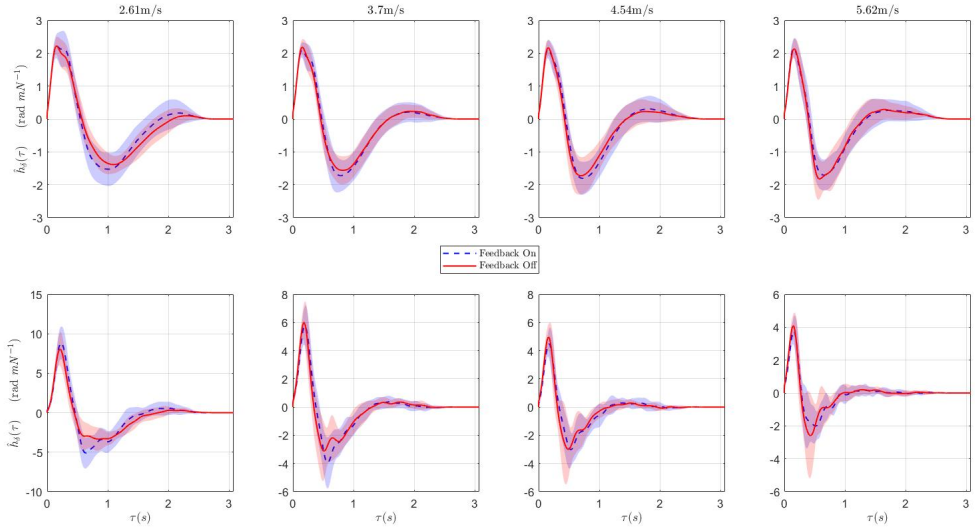


Figure 2.4: The impulse response function of the mean rider for steer angle (δ) and roll angle (ϕ). The shaded area represents the values within one standard deviation of the mean.

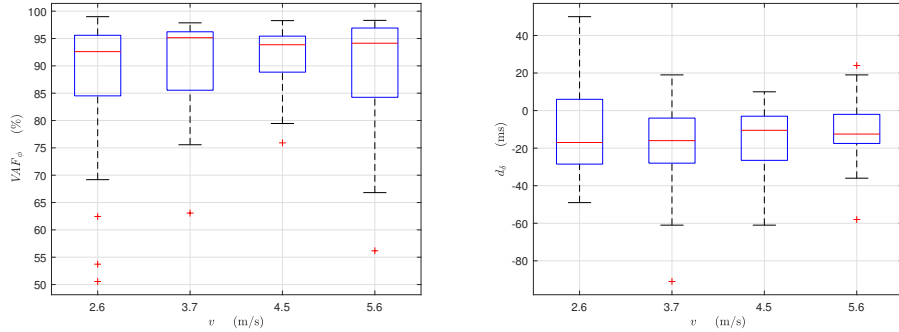


Figure 2.5: a) Box plot of variance accounted for between roll angle impulse response functions for all speed levels. b) Box plot of the relative delay in the estimated steering angle response between the two experimental conditions. Negative value means that the "feedback on" signal is delayed compared to the "feedback off".

comparison to the "feedback off". This might be due to the fact that the handlebars are more inert due to the additional steering feedback.

The lateral pull disturbances can be translated into a lean torque in the direction of forward speed and a steer torque in the direction of the steering axis. This means that any dynamic effects that influences these torques must be examined. The performance of the steer-by-wire controller was examined by numerical simulation and subjective measurements. All subjects reported that they felt like riding a mechanically steered bicycle, no adaptation period was required before the experiments. During the experiments very little motion of the upper body was evident and steer control was expected to be the main mechanism for bicycle balance [13]. Thus, we assume that the intrinsic and reflexive responses of the upperbody do not affect the validity of these results.

Physiologically there are two ways in which proprioception works in order to give the rider information regarding the state of the front assembly. First are the muscle spindles which by detecting changes in velocity and position of the shoulder joint give the rider an estimation of the steering angle and steering rate of the handlebars. Second are the Golgi tendon organs which work as force feedback sensors. The sensory information provided by the latter sensor is what this experiment tried to invalidate. In the feedback on case, information from the ground reaction torque of the front tire is transferred through the handlebars to the sensory receptors of the rider arms and is used for further state estimation. In the feedback off case the steer-

ing feedback information is lost.

Despite the change in the dynamics of the upper handlebar the response of the rider is almost identical. Thereupon, we assume that the internal controller of the rider is either adaptive or is driven by some combination of torque or position control. In the case of torque control this would mean complete re-adaptation of feedback gains which would have resulted in some kind of adaptation period for the participants when they swapped steering configurations. Although, no adaptation period was needed for any of the participants. Alternatively, in the case of position control steer angle increments are feed-through an inverse model of the steering assembly to produce the necessary forcing element. In this case, switching between configurations, would mean re-adaptation of the internal model of the handlebar assembly. This is much more plausible as it mainly concerns tuning of the internal perception of handlebar inertia which can happen instantaneously. To reveal if the later assumption is true an additional study that models the rider as position and torque controller will be conducted. The identified parameters of the former and later controller might lead into further insights regarding the conclusions of this study.

All data and supplemental material related to this article is available online at <https://doi.org/10.5281/zenodo.3365351> (Dialynas et al., 2019).

3

A GRAY BOX ANALYSIS ON THE EFFECT OF TORQUE FEEDBACK DURING CYCLING UNDER LATERAL PERTURBATIONS

3.1. INTRODUCTION

In the lateral perturbation experiments conducted for two experimental conditions (torque feedback on and off), a statistical significant difference for control effort and task performance could not be discerned. This indicated that the rider despite the reduced feedback and changed bicycle dynamics managed to compensate and produce similar outputs. For this reason, a gray box analysis is conducted in this work to get further insights on what and why might have led to the findings derived in [4].

3.2. METHODS

1. Black box identification : the procedure described in [4] is followed to produce impulse response functions (IRFs), thorough the use of a FIR model, for steering angle δ , roll angle ϕ , yaw angle ψ and steer torque T_δ . In the case of T_δ instead of considering the whole bicycle rider closed loop system as a black box, the bicycle rider open loop is chosen with input the disturbance w and output the control input T_δ .
2. The produced IRFs $h^\delta(\tau)$, $h^\phi(\tau)$, $h^\psi(\tau)$, $h^{T_\delta}(\tau)$ are filtered using zero-phase low pass filter with a cutoff frequency of 10 Hz.
3. The IRFs are averaged over all participants in order to produce the mean rider response. The variance accounted for VAF between each individual's response and the mean rider's is calculated. The rider with the highest VAF across all speed levels is chosen as the median rider. All further analysis is conducted on the response of the median rider.
4. The IRFs of the median rider are convolved with the measured disturbances of each run to produced the filtered output $y_\delta(t)$, $y_\phi(t)$, $y_\psi(t)$, $y_{T_\delta}(t)$.
5. Zero Delay Model gray box identification: A gray box model is fit to the measured lateral force and the filtered response of the FIR model for each run. This is repeated for three conditions. In the first, the control process dynamics approximate a normal bicycle and are similar to the experimental condition described in [4] and referred to as haptic feedback on (haptics on), while the rider has the torque feedback loop connected. In the second, the control process dynamics approximate again a normal bicycle, but the internal torque feedback loop of the rider is severed. In the third the steering configuration dynamics change to simulate the experimental conditions described in [4] and referred to as haptic feedback off (haptics off) but the rider's internal torque feedback loop is present.
6. Variable Delay Model gray box identification: The model is updated with time delays. The model is fit to the measured lateral force and the filtered response of the FIR model for each run. This is repeated for

the three conditions described above.

7. Reafferent Optimal Prdiction (ROP) Model gray box identification: The gray box model is updated with a delay compensation algorith. The model is fit to the measured lateral force and the filtered response of the FIR model for each run. This is repeated for the three conditions described above.
8. Assessment on the importance of torque feedback is made based on the the covariance of the identified gray box parameters and the change of *VAF* in the lateral force to steer angle fit between conditions.
9. Assessment on the delay compensation strategy used is made based on the fitting perfomance accross gray box models. Additionally the predictor is compared with a more conventional apporach found in motor control literature.

3.2.1. BICYCLE MODEL

The bicycle model used is the so called Whipple-Carvalho model the dynamics of which have been expressed in a set of linearized equations by Meijaard et al. [11]. In the original model three assumptions are made. The first is that the rider is rigidly attached in the saddle with the mass of the arms and legs acting as a point. Secondly, the contact between tire and ground is modelled as a non slipping rolling point contact meaning that the wheels can rotate without lateral slip. Lastly it is assumed that the total energy of the system is preserved. The resulting non-holonomic mechanical model has three velocity degrees of freedom, the forward speed, the rear frame roll rate $\dot{\phi}$ and the steering rate $\dot{\delta}$. The lateral motion is described by two coupled second order

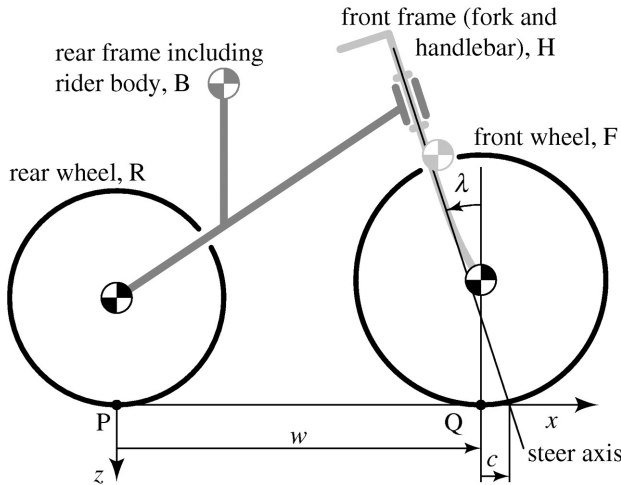


Figure 3.1: The Whipple-Carvalho bicycle model consists of four rigid bodies: rear wheel R, rear frame B, front frame H and front wheel F connected via hinges. The center of mass locations are expressed relative to the x - and z -coordinates shown (with origin at P and y pointing towards the reader). The other parameters shown are the steer axis tilt λ , wheelbase w and trail c . The model at its most expanded form is described by 25 parameters.[11]

differential equations given by equation (3.1).

$$\mathbf{M}\ddot{\mathbf{q}} + \nu\mathbf{C}_1\dot{\mathbf{q}} + [g\mathbf{K}_0 + \nu^2\mathbf{K}_2]\mathbf{q} = \mathbf{f} \quad (3.1)$$

where \mathbf{q} is a vector containing the roll and steer angles, \mathbf{f} is a vector containing the roll and steer torques, g is the gravitational acceleration and \mathbf{M} , $\nu\mathbf{C}_1$, $g\mathbf{K}_0 + \nu^2\mathbf{K}_2$ are the "mass", "damping" and "stiffness" ratios in matrix form respectively. The entries in the constant coefficient matrices $\mathbf{M}, \mathbf{C}_1, \mathbf{K}_0, \mathbf{K}_2$ are calculated from a set of 25 bicycle parameters related to inertial and design properties of the steer by wire bicycle (see table 3.4).

To determine the stability of the open loop system in a straight ahead motion the characteristic polynomial derived from

$$\det(\mathbf{M}\lambda^2 + \nu\mathbf{C}_1\lambda + g\mathbf{K}_0 + \nu^2\mathbf{K}_2) = 0 \quad (3.2)$$

is solved for a forward speed range from 0 to 10 ms⁻¹ where λ are the eigenvalues of the system (see figure 3.2). The two interesting eigenmodes defined by the locus plot are the weave and capsise. The weave

corresponds to an oscillatory mode as can be seen by the existence of imaginary parts and represents a motion in which the bicycle sways about its heading. The oscillatory motions exponentially fades when forward speed is larger than 4.39 m s^{-1} . The capsizing on the other hand has an eigenvector dominated by lean and leads to a gradual roll drift to infinity when the eigenvalue crosses the zero line around 6.67 m s^{-1} . Since in

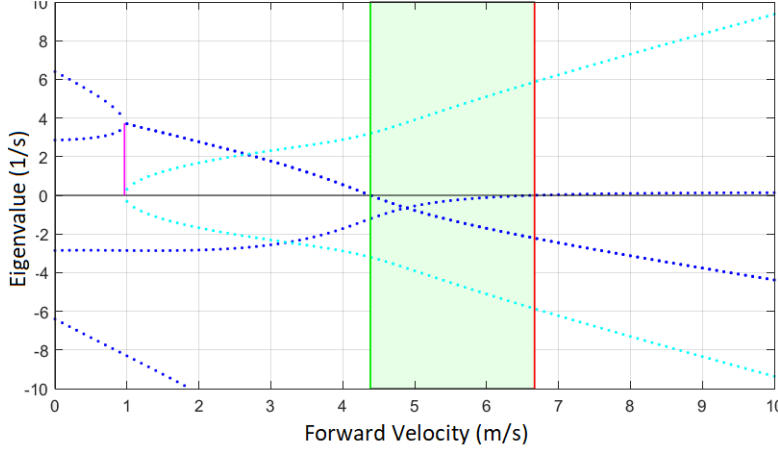


Figure 3.2: Root locus plot of the steer by wire bicycle. Dotted blue lines indicate the real part of the eigenvalues while dotted cyan show the imaginary part. The stable region corresponds to speeds $4.39 \lesssim v \lesssim 6.67 \text{ m s}^{-1}$

the experimental setup the task could not be isolated to purely balance the equations are extended to include heading. Heading is defined as a linear combination of steer angle and steer rate as expressed by Meijaard et al. [11] in equation (3.3).

$$\dot{\psi} = \frac{v\delta + c\dot{\delta}}{w} \cos \lambda \quad (3.3)$$

When modelling the feedback off case of the steer-by-wire bicycle the dynamics of the plant need to change accordingly. In that configuration the forcing steering input is directly proportional to steering acceleration times the inertia of upper handlebar assembly, for this reason the second of the set of equations in 3.1 is replaced by:

$$I_{Fxx}\ddot{\delta} = T_\delta \quad (3.4)$$

For control purposes equation (3.1) is expressed in state space form with state vector $\mathbf{x} = [\dot{\phi}, \dot{\delta}, \phi, \delta, \psi]^T$, forcing input $\mathbf{f} = T_\delta$ and output equal to the full state. The bike is assumed to be controlled only by a steering torque because according to both Moore [14] and Weir [21] the rear frame roll angle is mainly controlled by steering.

$$\dot{\mathbf{x}} = \mathbf{A}\mathbf{x} + \mathbf{B}T_\delta + \mathbf{H}_d w \quad (3.5)$$

$$\mathbf{y} = \mathbf{C}\mathbf{x} + \mathbf{D}\mathbf{f} \quad (3.6)$$

where matrices A, B, C, D, H_d are defined by:

$$\mathbf{A} = \begin{bmatrix} -\mathbf{M}^{-1}v\mathbf{C}_1 & -\mathbf{M}^{-1}(g\mathbf{K}_0 + v^2\mathbf{K}_2) \\ \mathbf{I}_2 & \mathbf{0} \\ 0 & \frac{ccos\lambda}{w} \\ \frac{ccos\lambda}{w} & 0 \end{bmatrix}, \mathbf{B} = \begin{bmatrix} \mathbf{M}^{-1} \\ \mathbf{0} \end{bmatrix} \quad (3.7)$$

$$\mathbf{C} = \mathbf{I}_5, \mathbf{D} = \mathbf{0} \quad (3.8)$$

$$\mathbf{H}_d = \begin{bmatrix} \mathbf{M}^{-1} \begin{bmatrix} l_g \\ c_s \end{bmatrix} \\ \mathbf{0} \end{bmatrix} \quad (3.9)$$

\mathbf{H}_d is the matrix defining the dynamics of the lateral disturbance w . In this case the force application point was l_g distance from the ground. The constant c_s is the fraction of w that results in a steering torque in the handlebar assembly.

3.2.2. RIDER CONTROL MODEL

In order to investigate the effects of the torque feedback loop attributed to the golgi tendon organs a rider control model is created. The complete high level overview of the model is shown in figure 3.3.

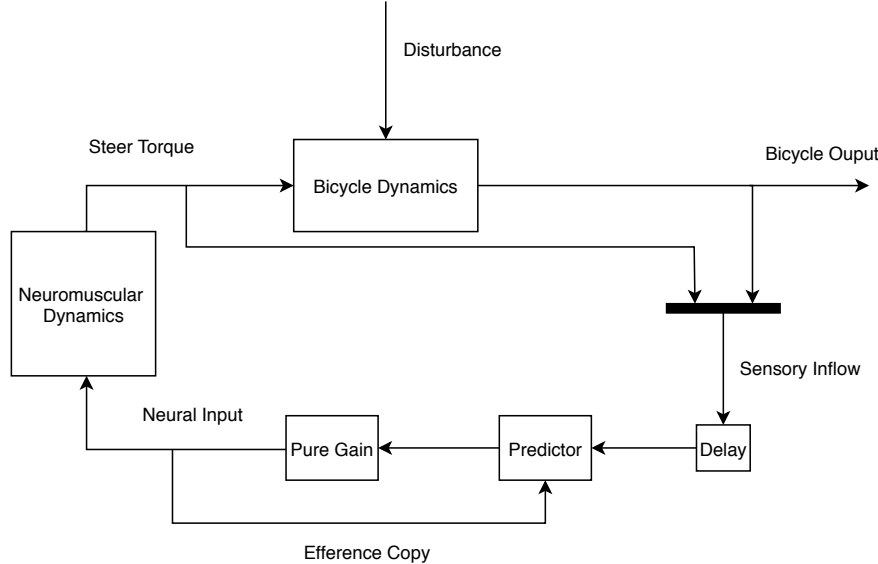


Figure 3.3: Block diagram of the complete rider-bicycle model.

The neuromuscular dynamics block works as a second order filter to simulate the limitations of the human response. In state space form this block is expressed by :

$$\dot{x}_{nm} = \begin{bmatrix} 0 & 1 \\ -\omega^2 & -2\zeta\omega \end{bmatrix} \begin{bmatrix} T_\delta \\ \dot{T}_\delta \end{bmatrix} + \begin{bmatrix} 0 \\ \omega^2 \end{bmatrix} a \quad (3.10)$$

$$y_{nm} = [1 \ 0] \begin{bmatrix} T_\delta \\ \dot{T}_\delta \end{bmatrix} \quad (3.11)$$

where ζ is the damping coefficient and ω_c is the cutoff frequency. These parameters were chosen according to activation dynamics present in the shoulder joint [6].

The steer angle and steer rate feedback is attributed to the muscle spindles, while the torque feedback is made possible with the help of the golgi tendon organs. The roll and heading angle come from the visual system. Lastly the roll rate feedback is attributed to the vestibular system.

The bicycle model of equation (3.5) is combined with the neuromuscular dynamics block of equation (3.11) to create a combined plant with state $x = [\dot{\phi}, \dot{\delta}, \phi, \delta, \psi, T_\delta, \dot{T}_\delta]^T$, input a and w and output $y = [\dot{\phi}, \dot{\delta}, \phi, \delta, \psi, T_\delta]^T$. In order to make possible the implementation of the predictor which is discrete in nature the state space representation of the combined plant is discretized with a time step of 0.001 s. The equivalent model block diagram is shown in figure 3.4.

THE REAFFERENT OPTIMAL PREDICTOR

Many strategies to counter time delays have been proposed in literature. The most basic predictor is the Smith Predictor, which has been explored in motor control research by Miall et al. [12]. The smith predictor compensates for time delays through the use of an internal forward model of the controlled dynamics and an internal model of the sensory delay pathways. The forward model works by utilizing an efferent signal of the control input while the comparison between prediction and measurement is trying to simulate the

human's ability to distinguish between reafference and exafference. Unfortunately the most basic smith predictor scheme does not work for unstable open loop systems [17]. In this work a modification to the normal smith predictor scheme is suggested. In place of the forward model an optimal tapped delay line is used that forward simulates the amount of steps according to the model of sensory delay. This works like a re-setting forward model that is updated every time step by the delayed state so the predictor loop does not become unstable. A tapped delay line without the smith correction can still work and has been implemented by van der Kooij et al. [19] for modelling stance control but it leads to predictions that do not contain any amount of the effect of the disturbance on the state. The predictor structure used in this work can be seen in figure 3.4.

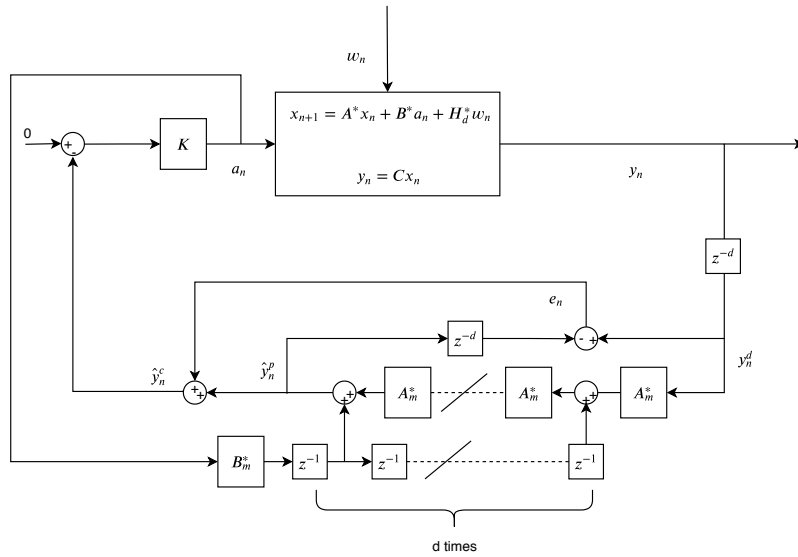


Figure 3.4: Equivalent block diagram of the bicycle-rider system in discrete time. A^* , B^* are the discretized matrices of the combined plant dynamics while d is the amount of time delay in number of time steps. The delayed output measurement is forwarded in time in the tapped delay line to produce the first undelayed estimate of the output \hat{y}_n^p , which is again delayed through a model of the time internal time delay. The difference between this re-delayed prediction with the delayed measurements creates the error e which is added back to \hat{y}_n^p to create the final corrected prediction \hat{y}_n^c

3.2.3. PARAMETER ESTIMATION

In order to assess the effectiveness of the torque feedback loop, three models of incremental complexity are used. In the first the feedback pathways are fed into the controller without delays. In the second delays are added. The third one compensates for time delays by the use of the predictor described above. The three models have the controller gains as free parameters. The gains are estimated by fitting the model output into the non-parametric data-set derived in [4]. The gains were estimated by minimization of the cost function

$$V_N(\boldsymbol{\theta}) = \frac{1}{N} \sum_{k=1}^N \left[5 \left(\hat{y}_k^\delta(\boldsymbol{\theta}) - y_k^\delta \right)^2 + \left(\hat{y}_k^\psi(\boldsymbol{\theta}) - y_k^\psi \right)^2 + 8 \cdot 10^{-4} \left(\hat{y}_k^{T\delta}(\boldsymbol{\theta}) \right)^2 \right] \quad (3.12)$$

where $\boldsymbol{\theta}$ is a vector containing all the free parameters, \hat{y}^δ and \hat{y}^ψ are the outputs of the simulation for the measured external disturbance w and the vector of parameters $\boldsymbol{\theta}$ for steer angle and heading angle respectively, while y^δ and y^ψ are the outputs of the non-parametric model and are calculated by convoluting the impulse response functions h^δ and h^ψ with the measured disturbance w respectively. The derivation of the non-parametric data-set is further explained in [4].

The first two terms of the cost function are trying to match the steering and heading response of the parametric model with that one of the non-parametric model, while the third one minimizes the amount of input torque generated in order to produce the best possible fit. The weights were chosen heuristically. For optimization the genetic algorithm with a fitness limit of 0.03 is first used in order to produce a good starting parameter vector for gradient descend algorithm to take over, which finally finds the closest possible estimate of the global minimum. For the genetic algorithm a crossover fraction of 0.85 along with a population size 10 times the length of the parameter vector is used. The gains attributed to the muscle spindle sensors (K_δ and $K_{\dot{\delta}}$) are constrained to be only positive. The assumption is that they work like a delayed steering stiffness and damping. Additionally, the parameters are constrained to fall under -250 and 250 so as to avoid unrealistically high gain values.

The impulse response function of the median rider is used. This is determined by taking the mean impulse response function of each measured output and finding the participant which had the highest variance accounted for between the individual response and the mean across all speed levels. Each system was identified for three different model conditions. In the first all six feedback pathways are used including torque feedback, on the second torque feedback is excluded from the model by assuming that its corresponding gain is zero. Finally in the third, six gains are again used but the plant dynamics are modified so as to simulate the feedback off case of the experimental condition as described in section 3.2.2. As metric of model validity the variance accounted for between parametric and non-parametric output is used, defined as

$$VAF_d(\boldsymbol{\theta}) = 1 - \sum_{k=1}^n \left(y^d(k) - \hat{y}^d(k, \boldsymbol{\theta}) \right)^2 / \sum_{k=1}^n \left(y^d(k) \right)^2 \quad (3.13)$$

where $d = \{\phi, \delta, \psi\}$.

In order to assess the importance of the torque feedback, the uncertainty of each parameter is found. Parameters with the lowest uncertainty contribute more to the fit so they are deemed more important. To find the uncertainty the covariance matrix is estimated from :

$$\text{cov}_{\hat{\boldsymbol{\theta}}} = V_N(\hat{\boldsymbol{\theta}}) \mathbf{H}(\hat{\boldsymbol{\theta}})^{-1} \quad (3.14)$$

$$\text{with } \mathbf{H}(\hat{\boldsymbol{\theta}}) = \frac{\partial^2 V_N}{\partial \theta_i \partial \theta_j} \quad (3.15)$$

where $\hat{\boldsymbol{\theta}}$ is the parameter the closest estimate to the true vector θ^* that produces the true global minimum and \mathbf{H} is the hessian matrix numerically estimated by the gradient descend algorithm. However, since bigger parameters are going to have naturally larger variances the diagonal values are normalized by the parameter value to produce the coefficient of variation.

$$CV_i = \sqrt{\frac{\sigma_{\hat{\theta}_i}^2}{\hat{\theta}_i^2}} \quad (3.16)$$

where $\sigma_{\hat{\theta}_i}^2$ are the diagonal elements of $\text{cov}_{\hat{\boldsymbol{\theta}}}$.

3.3. RESULTS

3.3.1. ZERO DELAY MODEL

The results of the zero delay model are presented in table 3.1. A fit of over 90 % is easily achieved for both steer angle and heading, while for roll the discrepancy is larger. A look into how the model approximates the measured rider input and bicycle states for the forward speed 3.6 m s^{-1} is seen in figure 3.5. The discrepancy in the roll angle fit can be explained by the fact that the model does not account for upper body motions which are expected to have a considerable impact on bicycle dynamics.

From the index of dispersion it is seen that the torque feedback gain $K_T\delta$ along with the steer rate gain $K_{\dot{\delta}}$ contribute most in the fit, since the consistently have the lowest uncertainty level among all parameters. Additionally, VAF_δ drops more than 15-20% when the feedback is turned off (see table 3.1). The steering angle response becomes significantly more oscillatory when the feedback is turned off (see figure 3.6). Roll

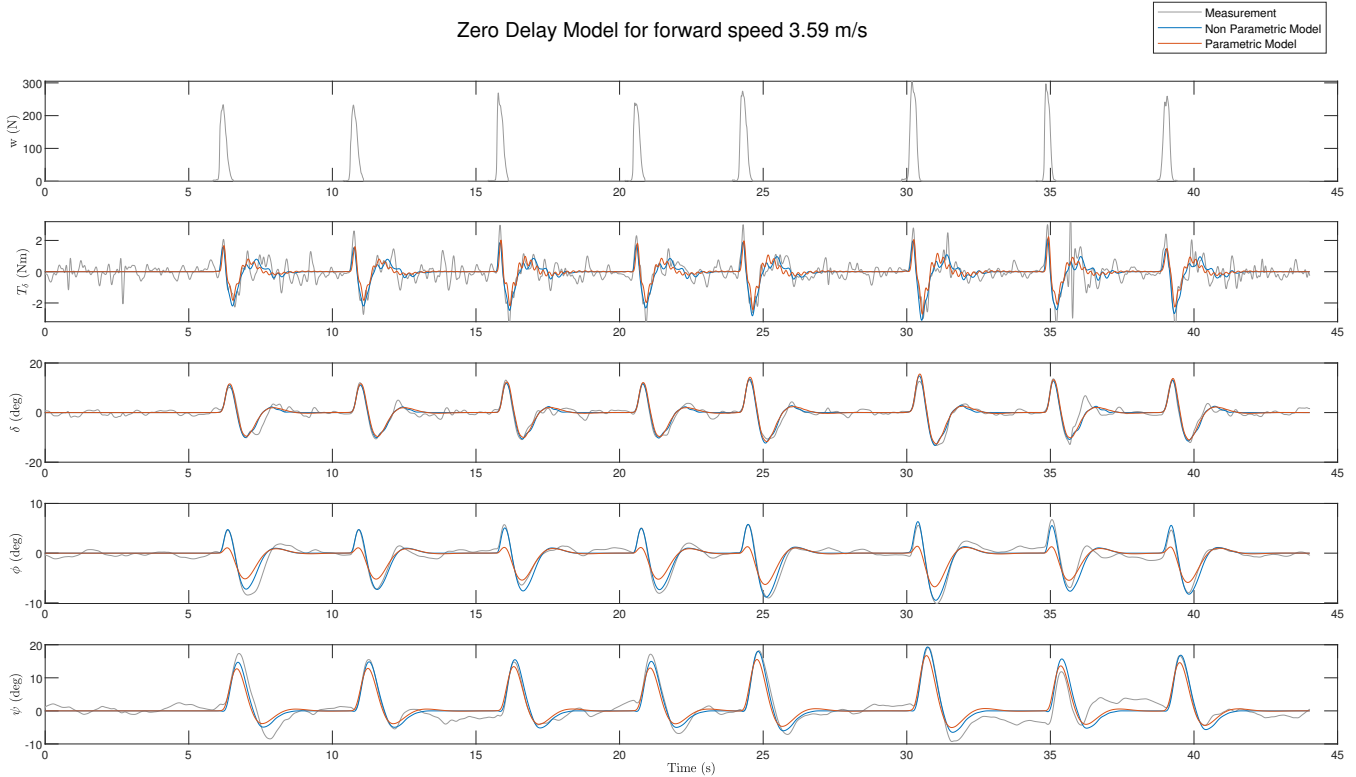


Figure 3.5: Comparison between parametric model output, non-parametric model output and measured signals for the speed level of 3.6 ms^{-1} for the case where torque feedback activated.

stabilization performance does not seem to be affected, however steering effort considerably does. Worth noting that in the experimental feedback off case the level of fit degradation is almost non existent.

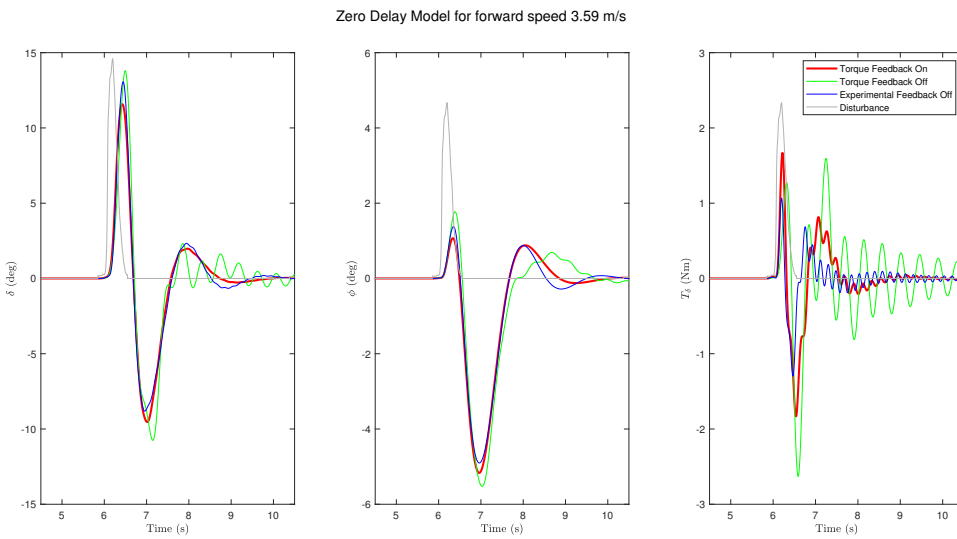


Figure 3.6: Steering, roll angles and input rider torque compared among torque feedback levels for the forward speed of 3.6 ms^{-1} . The disturbance signal is not shown to scale.

3.3.2. VARIABLE DELAY MODEL

The same procedure was repeated for the model but now introducing delays in all feedback pathways. For δ and $\dot{\delta}$ which are attributed to the muscle spindle sensors and for the torque feedback which is attributed to the golgi tendon organs a delay of 25 ms is chosen [3, 18]. For the feedback states attributed to visual feedback such as the roll angle ϕ and yaw angle ψ a much greater delay of 200 ms is chosen. Finally for the vestibular roll rate feedback a delay of 50 ms is implemented [1].

The results of the variable delay model are presented in table 3.2. Despite the fact that significant delay is introduced into the system the torque feedback loop manages to compensate maintaining a VAF_δ of over 90 % for low speed levels (see table 3.2 and figure 3.7). In figure 3.8 the delayed response of the rider is visible between the dotted red and bold red line. This is further exaggerated in the two remaining conditions resulting in much more oscillatory steering responses with a visible impact on roll stabilization. The index of dispersion follows similar pattern as in the zero delay model, with the proportional heading and roll gains having the largest uncertainty while the steer rate and torque feedback gain having the lowest. Between feedback on and feedback off, a much larger drop in VAF is noted. Additionally, a equally significant drop in the fit is noted for the experimental feedback off case, which was not present in the zero delay model.

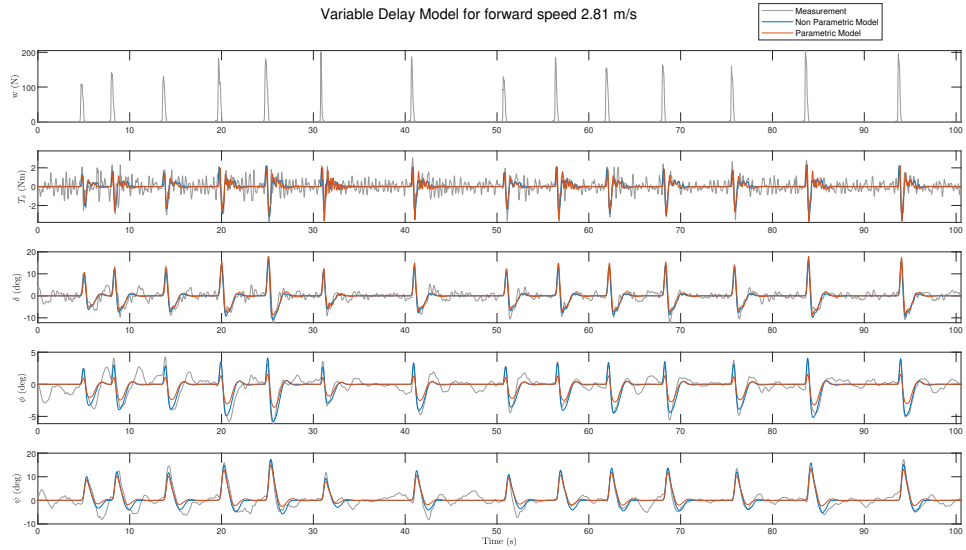


Figure 3.7: Comparison between variable delay model output, non-parametric model output and measured signals for the speed level of 2.8 m s^{-1} for the case where torque feedback is activated.

3.3.3. FINAL MODEL

The final model of figure 3.4 is implemented with a consistent time delay among sensory pathways equal to 50 ms. Adaptation of the predictor to work with variable time delays is not part of the scope of this work. It is assumed that the internal model of bicycle and neuromuscular dynamics along with the internal model of the inherent time delay responsible for prediction is perfect for controlling the normal bicycle dynamics. However in the experimental off, where the steering dynamics change, the internal model is not updated in simulation on purpose. This falls inline with what was noted during the experiments where the subjects adapted to the new bicycle dynamics instantaneously, so a full "re-calibration" of the forward model is too far fetched. This way the extent to which the smith prediction principle can counter forward model inaccuracies is also tested.

The optimization results for the final model are presented in ???. From the $VAFs$ and the signals shown in figure 3.9 it is visible that the quality of the fit is comparable with the ideal zero delay case. The index of dispersion follows similar trends with the two previous models with K_δ being the most important for the fit as it has the lowest uncertainty. The drop between feedback conditions is also similar to the zero delay case. Furthermore, the steering response exhibits the same oscillatory behaviour when torque feedback is completely disabled. However, the predictor manages to compensate in the feedback off experimental case

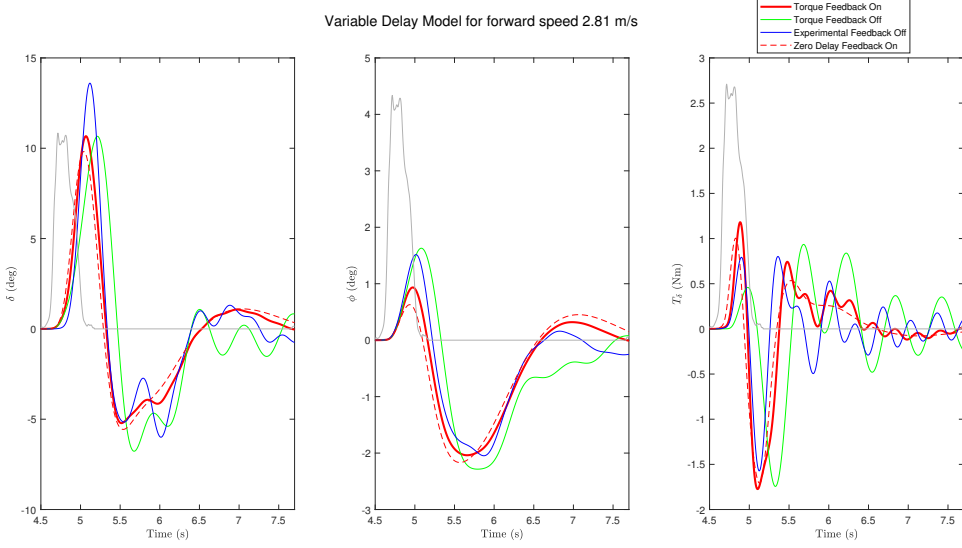


Figure 3.8: Steering, roll angles and input rider torque of the variable delay model compared among torque feedback levels for the forward speed of 2.8 ms^{-1} . The disturbance signal is not shown to scale.

and achieve good fit which was not present in the model with uncompensated time delays.

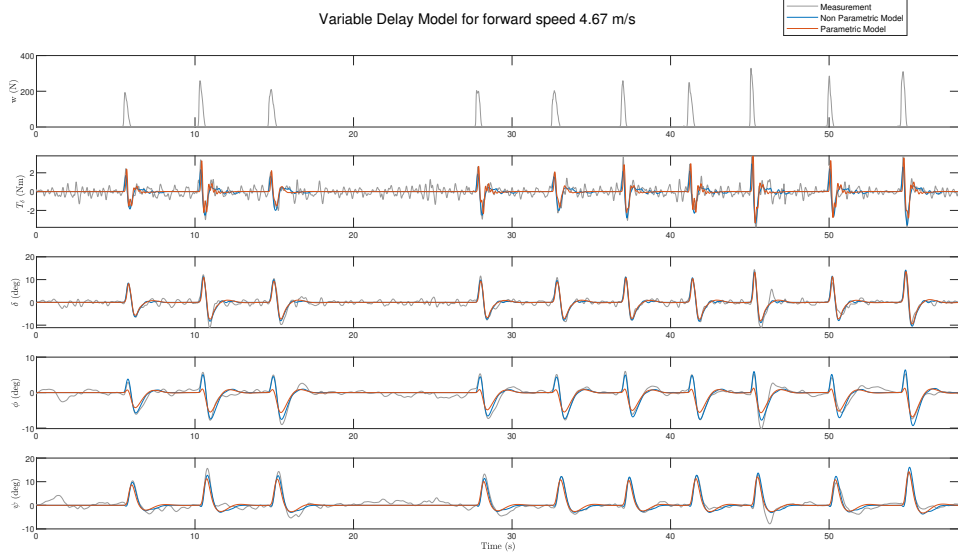


Figure 3.9: Comparison between variable delay model output, non-parametric model output and measured signals for the speed level of 4.67 m s^{-1} for the case where torque feedback is activated.

In figures 3.11 to 3.12 a complete comparison between rider models for all feedback conditions is presented. The response shown is the result of the first lateral perturbation of each individual run. The zero delay and prediction models exhibit almost identical responses as it was evident from the over 90% fit achieved. The variable delay model lags behind in both the produced control input and bicycle output, as is expected. Worth noting the lag in the control input of the prediction model in the first few milliseconds after the perturbation. Despite that fact the model compensates and achieves similar output as the idealized zero delay case. This is a result of the fact that no matter how good the prediction algorithm is the human has no knowledge of the future so the response from the controller will start after the first state information arrives from the feedback pathways which are delayed. The forward model in this case does not help predict the state as it has no

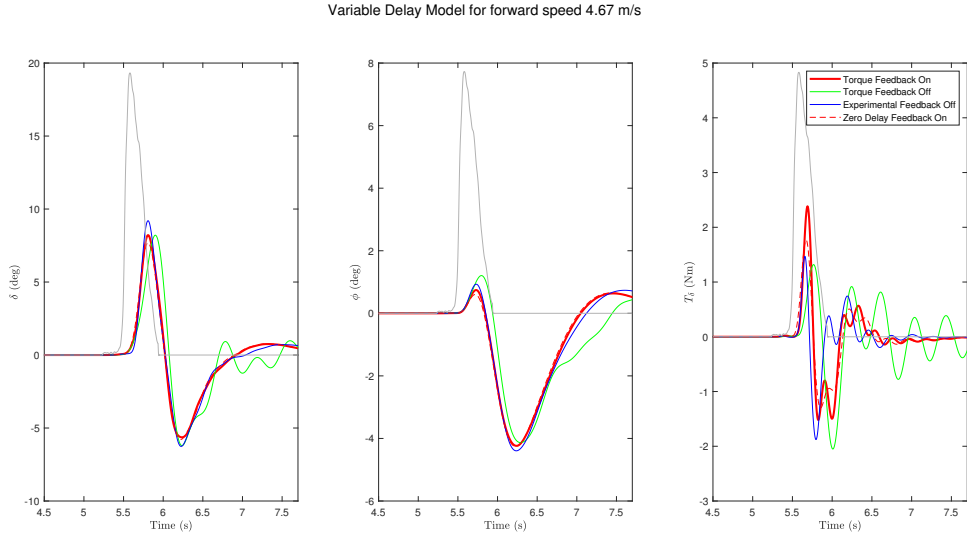


Figure 3.10: Steering, roll angles and input rider torque of the variable delay model compared among torque feedback levels for the forward speed of 4.67 ms^{-1} . The red dotted line is the feedback on case of the zero delay model and is shown for reference. The disturbance signal is not shown to scale.

information of the external disturbance.

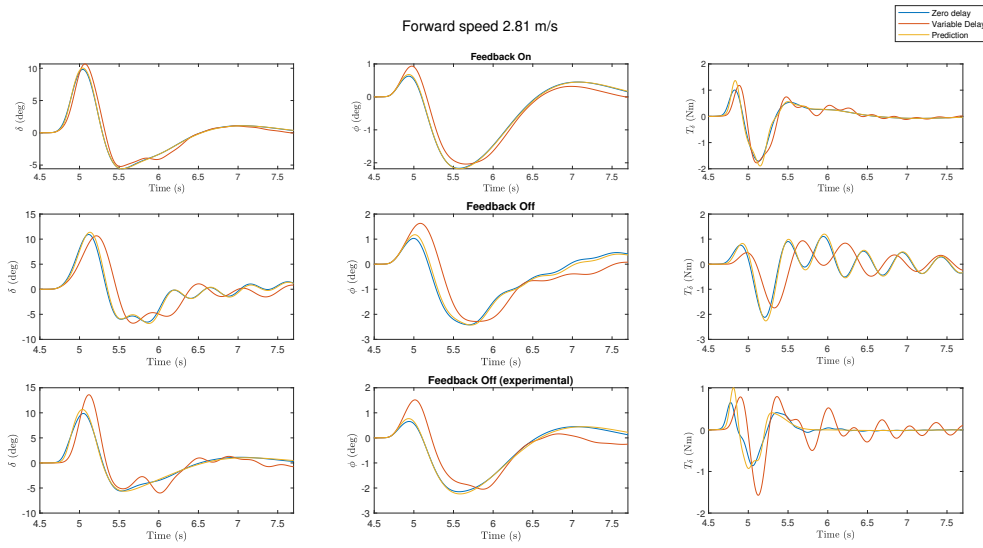
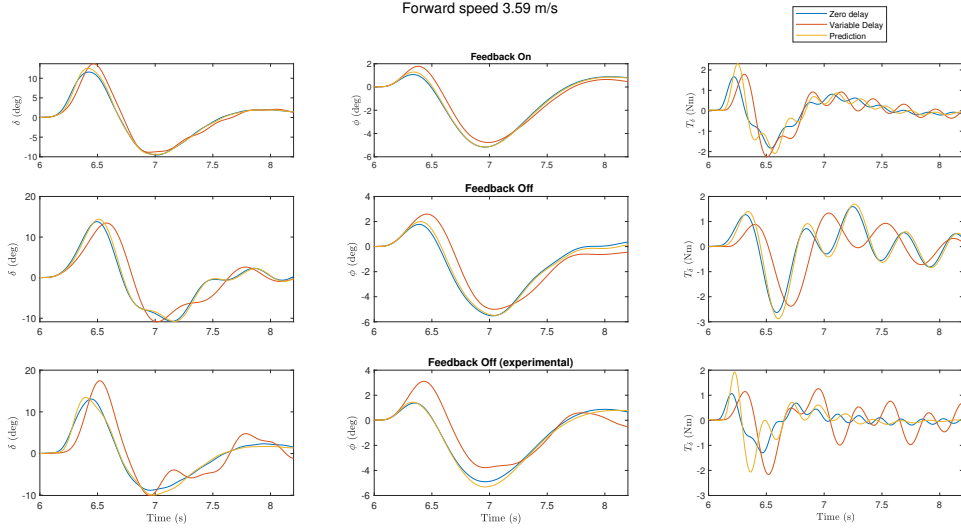
3.4. DISCUSSION

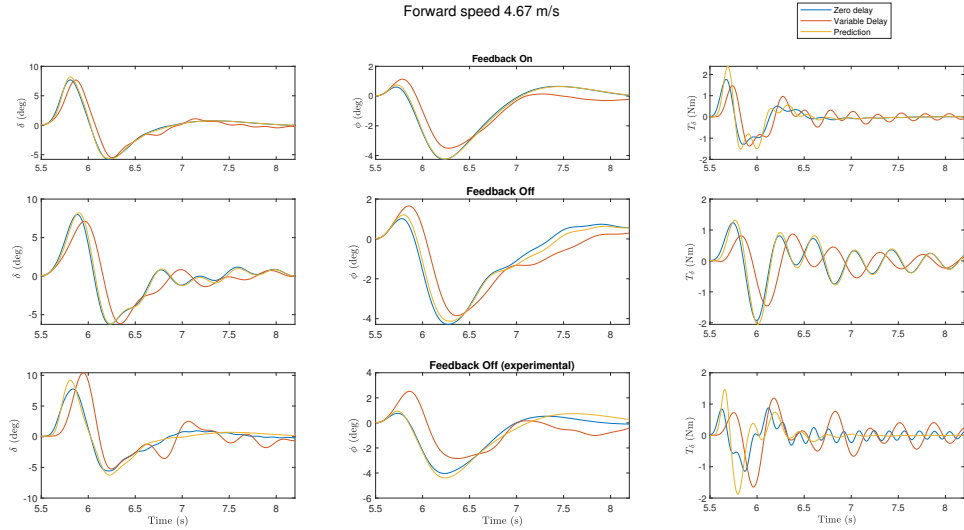
Since in the control scheme the feedback is defined as negative, positive feedback gains produce torques opposite to the direction of the state that they act on. For example positive K_δ acting on the steering angle signal will lead to torques that always try to make steering angle equal to zero. This was a design choice for all gains related to muscle spindles, in order to simulate lower spinal reflexes which lead to increased stiffness and damping of the handlebar assembly. This is the reason the index of dispersion for the gain K_δ is so large for the cases where the estimate is near zero (see table 3.2). The gradient descent algorithm if left unbounded would result in values lower than zero which would lead to a physiologically impossible reflex response.

On the other hand, the proportional and derivative roll gains are consistently negative among all models for all forward speeds and all torque feedback level conditions. This falls in line with what is believed to be the main balancing strategy for single track vehicles; the so called "steer into the fall". K_ψ always being negative means that the rider steers into the direction that heading is diverging, which seems counter intuitive. However, this can be explained by the fact that the heading correction task and the roll stabilization are inherently coupled. K_ψ also exhibits a consistent trend in all feedback conditions in all the rider models test. It decreases as the forward speed increases.

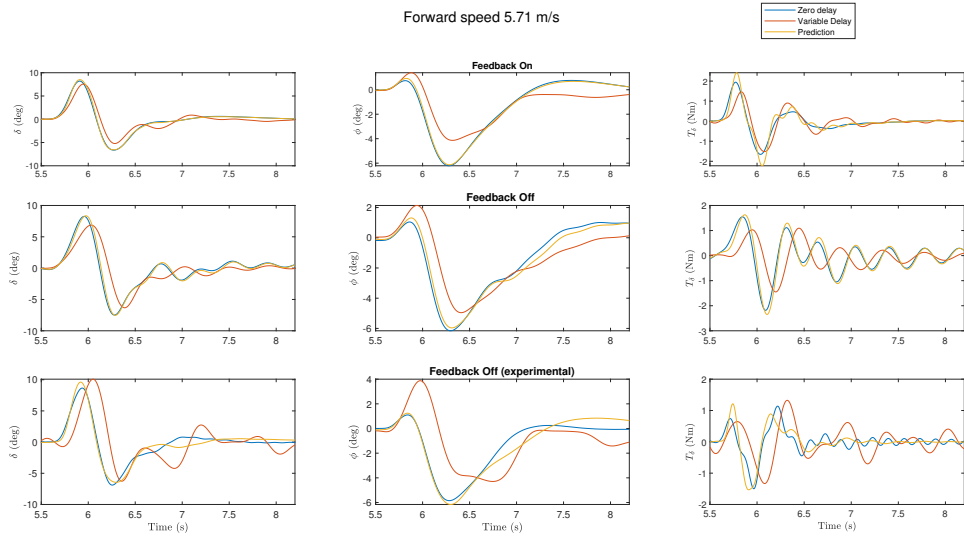
While the assumption that steering is the only active control input for the task of bicycle roll stabilization is correct, a secondary task is not taken into account by leaving the upper body unconstrained, which revolves around balancing of the torso and head. As a result, VAF_ϕ never reaches values higher than 85 %. This assumption was confirmed by performing a non linear model simulation, where bicycle and rider were modelled as two inverted pendulums with torsional spring and dampers in the two hinges. It was found that when a controller that tries to keep the center of mass of the upper pendulum constant, was activated the lean of the lower pendulum got worse. Consequently, the degree to which the rider can extrapolate information from their vestibular system to make deductions on the state of the bicycle is debatable, since the vestibular system measures roll rate and acceleration of the head and not the actual bicycle frame. However since this remains constant among conditions, the effectiveness of the torque feedback loop will remain analogous.

The torque feedback gain seems to be one of the two parameters that contribute most towards the fit; the other being the derivative steer angle gain. This is both indicated by the low index of dispersion and the fact that when the torque feedback loop is severed VAF_δ drops significantly. Even in the variable delay model,

(a) Comparison between the three rider models for forward speed 2.81 ms^{-1} (b) Comparison between the three rider models for forward speed 3.6 ms^{-1} Figure 3.11: Steering angle δ , roll angle ϕ and steering torque T_d compared among the three rider models implemented for all torque feedback conditions, for the two lowest speed levels.



(a) Comparison between the three rider models for forward speed 4.67 m s^{-1}



(b) Comparison between the three rider models for forward speed 5.71 m s^{-1}

Figure 3.12: Steering angle δ , roll angle ϕ and steering torque T_δ compared among the three rider models implemented for all torque feedback conditions, for the two highest speed levels.

Table 3.1: Results for the zero delay model as estimated for the median rider for all speed levels. Results are presented for the three conditions. Haptic on/off differentiates based on the dynamics of the bicycle model, while "with or w/o T_δ feedback" differentiates based on the structure of the rider control model. The values of the gains are presented as well as their corresponding uncertainty level measured by the coefficient of variation CV_i . Additionally, the variance accounted for of the orientation outputs between parametric and non parametric signals is also presented. The derivative gains ($K_{\dot{\phi}}, K_{\dot{\delta}}$) are measured in $\text{kgm}^2 \text{s}^{-2}$ while the proportional gains (K_ϕ, K_δ, K_ψ) are measured in $\text{kgm}^2 \text{s}^{-1}$. The torque feedback gain K_{T_δ} is dimensionless.

Forward Speed	Rider →	Bicycle →		Haptic On		Haptic Off	
		Value	CV (10^{-4})	Value	CV (10^{-4})	Value	CV (10^{-4})
2.8 ms^{-1}	$K_{\dot{\phi}}$	-77.17	114.86	-22.46	29.77	-115.36	213.52
	$K_{\dot{\delta}}$	2.26	73.57	2.58	18.93	8.76	187.30
	K_ϕ	-164.88	132.25	-24.50	73.14	-248.24	217.05
	K_δ	32.75	150.14	3.76	140.96	29.67	215.07
	K_ψ	-63.22	133.29	-9.85	53.71	-93.44	223.02
	K_{T_δ}	3.51	176.20	-	-	7.53	223.83
	VAF_ϕ	77.80		82.79		78.37	
	VAF_δ	98.34		79.19		98.20	
	VAF_ψ	93.46		93.51		93.74	
3.6 ms^{-1}	$K_{\dot{\phi}}$	-109.94	146.98	-21.30	35.99	-78.28	61.00
	$K_{\dot{\delta}}$	8.22	139.00	3.30	24.78	9.09	51.11
	K_ϕ	-248.47	147.39	-34.64	71.54	-229.14	84.40
	K_δ	50.78	147.72	6.48	130.57	53.16	92.96
	K_ψ	-132.13	152.08	-17.74	61.92	-103.75	74.49
	K_{T_δ}	4.52	167.24	-	-	6.89	64.17
	VAF_ϕ	79.92		85.93		80.89	
	VAF_δ	98.83		86.40		97.08	
	VAF_ψ	95.33		97.95		95.15	
4.7 ms^{-1}	$K_{\dot{\phi}}$	-92.50	117.34	-27.29	46.40	-102.63	40.87
	$K_{\dot{\delta}}$	4.81	183.05	4.25	41.56	11.24	28.38
	K_ϕ	-183.03	135.64	-38.17	76.43	-249.74	74.10
	K_δ	22.57	237.51	2.65	591.87	63.36	88.33
	K_ψ	-165.42	126.89	-33.78	63.74	-188.67	58.81
	K_{T_δ}	3.42	174.23	-	-	8.98	13.88
	VAF_ϕ	77.03		83.06		78.60	
	VAF_δ	97.57		80.27		95.57	
	VAF_ψ	91.41		97.03		92.48	
5.7 ms^{-1}	$K_{\dot{\phi}}$	-83.90	117.61	-31.12	43.99	-76.30	47.12
	$K_{\dot{\delta}}$	5.83	142.87	5.58	40.62	10.91	30.23
	K_ϕ	-166.08	127.89	-43.64	67.14	-208.33	83.09
	K_δ	14.85	98.10	1.14	1836.39	79.44	75.47
	K_ψ	-186.77	128.56	-49.82	52.31	-176.96	69.82
	K_{T_δ}	3.24	185.07	-	-	8.45	29.67
	VAF_ϕ	79.17		84.03		80.30	
	VAF_δ	97.51		84.09		94.71	
	VAF_ψ	90.97		96.41		91.56	

Table 3.2: Results for the variable delay model as estimated for the median rider for all speed levels. Results are presented for the three conditions. Haptic on/off differentiates based on the dynamics of the bicycle model, while "with or w/o T_δ feedback" differentiates based on the structure of the rider control model. The values of the gains are presented as well as their corresponding uncertainty level measured by the coefficient of variation CV_i . Additionally, the variance accounted for of the orientation outputs between parametric and non parametric signals is also presented. The derivative gains (K_ϕ, K_δ) are measured in $\text{kgm}^2 \text{s}^{-2}$ while the proportional gains (K_ϕ, K_δ, K_ψ) are measured in $\text{kgm}^2 \text{s}^{-1}$. The torque feedback gain K_{T_δ} is dimensionless.

Bicycle →		Haptic On			Haptic Off	
Rider →	with T_δ feedback	w/o T_δ feedback		with T_δ feedback		
Forward Speed	Value	CV (10^{-4})	Value	CV (10^{-4})	Value	CV (10^{-4})
2.8 m s^{-1}	K_ϕ	-68.53	38.72	-14.93	37.52	-28.19
	K_δ	2.09	110.32	2.30	32.17	2.65
	K_ϕ	-146.29	72.07	-16.98	92.51	-79.20
	K_δ	22.18	95.38	4.62	103.75	10.51
	K_ψ	-40.34	56.18	-3.78	116.84	-14.53
	K_{T_δ}	3.52	64.80	-	-	2.59
	VAF_ϕ	81.15		69.61		80.01
	VAF_δ	93.43		23.34		66.84
	VAF_ψ	93.78		69.67		83.30
3.6 m s^{-1}	K_ϕ	-51.02	56.62	-15.40	55.90	-21.25
	K_δ	2.50	170.45	2.81	50.20	2.79
	K_ϕ	-120.51	85.28	-22.82	102.83	-76.41
	K_δ	16.58	153.27	3.94	243.76	17.14
	K_ψ	-43.06	79.41	-7.37	147.32	-13.30
	K_{T_δ}	3.42	62.79	-	-	3.09
	VAF_ϕ	82.85		79.48		73.14
	VAF_δ	91.63		53.29		52.83
	VAF_ψ	95.10		84.88		71.58
4.7 m s^{-1}	K_ϕ	-51.78	64.60	-19.26	349.70	-14.88
	K_δ	2.75	160.68	4.42	438.96	3.04
	K_ϕ	-136.22	105.15	-27.02	111.78	-48.91
	K_δ	3.21	1156.00	0.01	492609.67	16.01
	K_ψ	-64.43	87.60	-14.29	412.99	-10.82
	K_{T_δ}	3.70	63.91	-	-	2.61
	VAF_ϕ	77.86		71.14		63.73
	VAF_δ	81.63		36.19		15.61
	VAF_ψ	90.32		80.57		55.71
5.7 m s^{-1}	K_ϕ	-38.58	136.91	-19.65	110.85	-10.10
	K_δ	1.13	2085.75	5.42	128.32	3.08
	K_ϕ	-120.59	120.57	-33.34	117.63	-30.95
	K_δ	0.00	3969013.40	0.01	280859.33	18.46
	K_ψ	-60.65	95.03	-19.20	183.00	-8.17
	K_{T_δ}	4.27	191.50	-	-	2.58
	VAF_ϕ	73.65		70.08		49.58
	VAF_δ	77.99		40.64		-
	VAF_ψ	84.32		79.50		39.90

Table 3.3: Results for the ROP model as estimated for the median rider for all speed levels. Results are presented for the three conditions. Haptic on/off differentiates based on the dynamics of the bicycle model, while "with or w/o T_δ feedback" differentiates based on the structure of the rider control model. The values of the gains are presented as well as their corresponding uncertainty level measured by the coefficient of variation CV_i . Additionally, the variance accounted for of the orientation outputs between parametric and non parametric signals is also presented. The derivative gains ($K_{\dot{\phi}}, K_{\dot{\delta}}$) are measured in $\text{kgm}^2 \text{s}^{-2}$ while the proportional gains (K_ϕ, K_δ, K_ψ) are measured in $\text{kgm}^2 \text{s}^{-1}$. The torque feedback gain K_{T_δ} is dimensionless.

Forward Speed	Rider →	Bicycle →		Haptics On		Haptics Off	
		Value	CV (10^{-4})	Value	CV (10^{-4})	Value	CV (10^{-4})
2.8 ms^{-1}	K_ϕ	-117.07	153.96	-21.11	30.98	-137.02	116.70
	$K_{\dot{\phi}}$	3.52	150.97	2.59	18.53	10.91	108.44
	K_δ	-248.50	159.45	-24.00	81.61	-249.38	118.66
	$K_{\dot{\delta}}$	47.43	167.35	4.39	131.79	23.39	153.29
	K_ψ	-94.42	161.46	-8.72	61.07	-97.63	119.57
	K_{T_δ}	5.26	190.30	-	-	10.13	113.01
	VAF_ϕ	78.78		82.85		80.41	
	VAF_δ	98.22		71.52		97.63	
	VAF_ψ	94.02		91.92		94.86	
3.6 ms^{-1}	K_ϕ	-103.91	220.15	-20.03	42.10	-129.88	125.12
	$K_{\dot{\phi}}$	7.55	205.98	3.28	31.80	17.90	126.50
	K_δ	-249.50	213.85	-32.88	85.42	-249.87	114.03
	$K_{\dot{\delta}}$	55.63	203.91	6.79	142.33	35.97	139.80
	K_ψ	-125.68	224.37	-15.64	66.86	-133.59	120.60
	K_{T_δ}	4.52	253.01	-	-	9.89	83.15
	VAF_ϕ	81.64		86.19		83.39	
	VAF_δ	98.02		80.82		97.11	
	VAF_ψ	96.21		97.09		97.15	
4.7 ms^{-1}	K_ϕ	-121.19	136.01	-25.17	54.75	-164.78	110.66
	$K_{\dot{\phi}}$	5.79	173.62	4.27	53.52	24.07	97.55
	K_δ	-247.23	131.94	-35.90	91.38	-249.79	102.96
	$K_{\dot{\delta}}$	36.74	151.80	4.18	433.29	17.36	324.16
	K_ψ	-214.97	140.95	-28.64	78.59	-238.76	112.77
	K_{T_δ}	4.84	155.81	-	-	13.11	80.91
	VAF_ϕ	79.31		82.12		81.74	
	VAF_δ	97.06		71.92		96.35	
	VAF_ψ	93.16		95.95		94.66	
5.7 ms^{-1}	K_ϕ	-111.38	131.04	-28.44	45.72	-150.97	93.00
	$K_{\dot{\phi}}$	6.57	126.55	5.57	44.04	32.07	82.12
	K_δ	-235.65	149.45	-40.32	86.47	-222.44	109.50
	$K_{\dot{\delta}}$	32.77	191.97	3.59	572.06	25.75	302.64
	K_ψ	-248.74	145.69	-41.87	65.89	-249.99	106.96
	K_{T_δ}	4.95	190.76	-	-	14.63	74.50
	VAF_ϕ	81.15		83.31		84.13	
	VAF_δ	97.11		75.79		94.72	
	VAF_ψ	92.70		96.05		95.41	

torque feedback was potent enough to compensate for the delays and achieve over 90 % fit in steering response for the lower forward speeds. This could be because torque inherently includes acceleration information and can give the controller a preview of how the rest of the state is going to evolve. However, in the experimental feedback off condition a degradation in fitting performance was only noted for the model with uncompensated time delays. In this case torque feedback is still proportional to the steering acceleration so the "preview" information is not completely lost. However the rider receives no input for the effect of the disturbance cause the torque that would naturally transfer through the front wheel contact point is filtered by the uncoupled fork-handlebar connection. Despite all that, in the final formulation of the model with prediction in place, the reduced torque information was not enough to negatively hinder the quality of the fit, which could explain why no difference was found between steering configurations in the experiments conducted in [4]. Furthermore the prediction strategy used manages to utilize the smith principle to enhance the optimal predictions of the tapped delay line with information of the effect of the disturbance on the state through reafferent pathways and simultaneously compensate for internal model inaccuracies. Note that in the feedback off experimental case the internal mode was not updated to reflect the changed dynamics, but the predictor manages to filter out the small discrepancies by comparing the forward model output with the delayed state measurements.

3.5. CONCLUSIONS

A gray box rider model was created that compensates for time delay by the use of a resetting internal forward model. The parameters were estimated through minimization of a cost function that both accounts for the riders concern towards performance and control effort. The results matched the measured non-parametric outputs derived in [4] with an acceptable level of fit. Contrary to what the initial conclusion might have been from looking at the results of the analysis done by Dialynas et al. [4], this work indicates that torque feedback is in fact crucial to the execution of the balancing task. Howeverm the torque feedback in the experimets was not physiologically neutered, as a result the remaining information was adequate for the rider to achieve comparable perfomance between conditions.

Table 3.4: Whipple model parameters for the steer-by-wire bicycle shown in figure.

Parameter	Symbol	Value
wheel base	w	$1.03m$
trail	c	$0.0665m$
steer axis tilt ($\pi/2 - \text{head angle}$)	λ	$\pi/10$
rear wheel	R	
radius	r_R	$0.6858m$
mass	m_R	$8.5 kg$
mass moment of inertia	(I_{Rxx}, I_{Ryy})	$(0.095625, 0.19125) kg m^2$
rear body and frame assembly	B	
position centre of mass	(x_B, z_B)	$(0.4, -0.6)$
mass	m_B	$95kg$
mass moment of inertia	$\begin{bmatrix} I_{Bxx} & 0 & I_{Bxz} \\ 0 & I_{Byy} & 0 \\ I_{Bxz} & 0 & I_{Bzz} \end{bmatrix}$	$\begin{bmatrix} 9.2 & 0 & 2.4 \\ 0 & 11 & 0 \\ 2.4 & 0 & 2.8 \end{bmatrix} kg m^2$
front handlebar and fork assembly	H	
position centre of mass	(x_H, z_H)	$(0.9, -0.66)$
mass	m_H	$1.5kg$
mass moment of inertia	$\begin{bmatrix} I_{Hxx} & 0 & I_{Hxz} \\ 0 & I_{Hyy} & 0 \\ I_{Hxz} & 0 & I_{Hzz} \end{bmatrix}$	$\begin{bmatrix} 0.05892 & 0 & -0.00756 \\ 0 & 0.06 & 0 \\ -0.00756 & 0 & 0.00708 \end{bmatrix} kg m^2$
front wheel	F	
radius	r_F	$0.6858m$
mass	m_F	$1.84kg$
mass moment of inertia	(I_{Fxx}, I_{Fyy})	$(0.097, 0.195) kg m^2$
battery rack	b	
position centre of mass	(x_b, z_b)	$(0.4, -0.55)$
mass	m_b	$4kg$
mass moment of inertia	$\begin{bmatrix} I_{Hxx} & 0 & I_{Hxz} \\ 0 & I_{Hyy} & 0 \\ I_{Hxz} & 0 & I_{Hzz} \end{bmatrix}$	$\begin{bmatrix} 0.02 & 0 & -0.02 \\ 0 & 0.04 & 0 \\ -0.02 & 0 & 0.02 \end{bmatrix} kg m^2$

A

CALIBRATION OF INERTIAL MEASUREMENTS

The fixed body angular velocities measured by the Inertial Measurement Unit (IMU) are biased due to the imperfect orientation of the sensor axis (see figure A.1). The goal is it to align system xyz with the global coordinate system XYZ. To achieve this the euler angle offsets are calculated by using the measurements from MPU-9050's built in accelerometer.

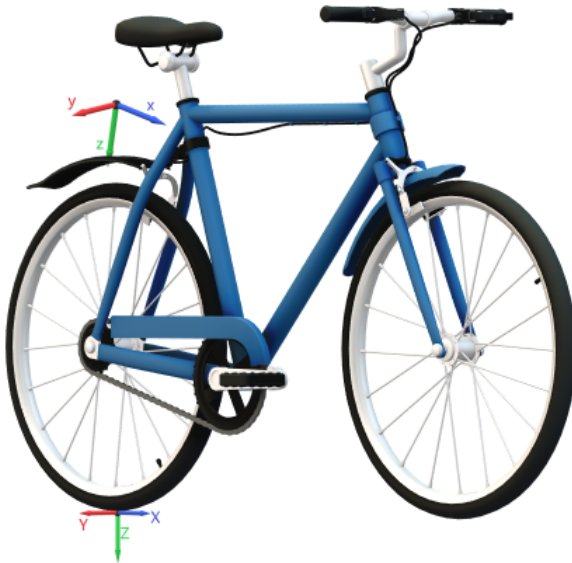


Figure A.1: Bicycle with body fixed sensor axis x-y-z (B) and global axis XYZ (G).

Different orders of rotation affects the end configuration. For this study the intrinsic order Z-Y'-X'' is adopted which is equivalent to the extrinsic X-Y-Z (roll-pitch-yaw). The inverse rotation matrix that described the above rotation sequence is :

$$R_{xyz} = R_x(\phi)R_y(\theta)R_z(\psi) = \begin{pmatrix} \cos\theta \cos\psi & \cos\theta \sin\psi & -\sin\theta \\ \cos\psi \sin\theta \sin\phi - \cos\phi \sin\psi & \cos\phi \cos\psi + \sin\theta \sin\phi \sin\psi & \cos\theta \sin\phi \\ \cos\phi \cos\psi \sin\theta + \sin\phi \sin\psi & \cos\phi \sin\theta \sin\psi - \cos\psi \sin\phi & \cos\theta \cos\phi \end{pmatrix} \quad (\text{A.1})$$

(a) Configuration $i = 1$ (b) Configuration $i = 2$

Figure A.2: a) The bicycle's desired Z axis is aligned with the vector of gravitational acceleration. The bike was validated to be completely upright by the use of a calibrated commercial IMU (MTw Awinda). b) The bicycle's desired X axis is aligned with the vector of gravitational acceleration. The door was validated to be completely vertical by the use of a calibrated commercial IMU (MTw Awinda). \mathbf{g} is the vector measured by the accelerometer which oposite to the gravitational acceleration.

where ϕ is the angle of rotation around axis X, θ is the angle of rotation around axis Y and ψ is the angle of rotation around axis Z. Equation (A.1) maps a vector from the global system G to the body fixed system B. In order to estimate the euler angle offsets the bike was configured in two different ways to align the gravity vector with the z and x axis respectively. The readings from the accelerometer are expressed in the sensor frame (B). Equation (A.2) is used to solve for the euler angle offsets. Unfortunately the three equations have only two degrees of freedom so two configurations are required so as to solve for all three angles.

In the first, $i = 1$ and $\mathbf{g}_1 = [0 \ 0 \ 1]^T$ (see figure A.2a) (note that the vector of accelerations is normalized) with equation (A.2) solving for θ and ϕ . The lack of any dependence on the yaw angle is intuitive to understand since a rotation around the z-axis is aligned with the gravitational field and accelerometers are completely insensitive to rotations about the gravitational field vector. Consequently in the second, $i = 2$ and $\mathbf{g}_2 = [-1 \ 0 \ 0]^T$ which leads to equation (A.2) solving for ψ and θ (see figure A.2b).

$$\frac{\mathbf{G}_i^B}{\|\mathbf{G}_i^B\|} = \begin{pmatrix} G_{ix}^B \\ G_{iy}^B \\ G_{iz}^B \end{pmatrix} \frac{1}{\sqrt{G_{ix}^{B^2} + G_{iy}^{B^2} + G_{iz}^{B^2}}} = \mathbf{R}_{xyz(\phi_o, \theta_o, \psi_o)} \mathbf{g}_i \quad (\text{A.2})$$

Solving equation (A.2) for the angles we get :

$$\phi_o = \tan^{-1} \left(\frac{G_{1y}^B}{G_{1z}^B} \right) \quad (\text{A.3})$$

$$\theta_o = \tan^{-1} \left(\frac{G_{1x}^B}{\sqrt{G_{1y}^B{}^2 + G_{1z}^B{}^2}} \right) \quad (\text{A.4})$$

$$\psi_o = \tan^{-1} \left(\frac{-G_{2y}^B}{\sqrt{G_{2x}^B{}^2 + G_{2z}^B{}^2}} \right) \quad (\text{A.5})$$

From equations (A.3) to (A.5) the euler angle offsets calculated are inserted into rotation matrix R_{xyz} . The transpose of the result (A.6) is then used to transform the IMU measurements from the coordinate frame B to the coordinate frame G which is consistent with the linearized equations of motion defined in ??.

$$R_{IMU} = R_{xyz}^T(\phi_o, \theta_o, \psi_o) = \begin{pmatrix} 0.9939 & -0.006106 & -0.1105 \\ 0.006069 & 1.0 & -0.000675 \\ 0.1105 & 0 & 0.9939 \end{pmatrix} \quad (\text{A.6})$$

B

ORIENTATION ESTIMATION FROM INERTIAL MEASUREMENTS

In order to properly assess the state of the bicycle when comparing it with the Whipple model, measurements of roll angle ϕ and yaw angle ψ are necessary. However the steer-by-wire bicycle has no way of measuring either. For this reason an estimation method is required that can approximate these angles by using measurements from already existing Inertial sensors. A distinction is made between methods that can estimate the euler angles when the whole signal is available for processing and for methods that can produce real-time estimation.

B.1. OFFLINE ESTIMATION METHODS

An estimation of the roll and yaw angle can be made by using the angular rates measured by the gyroscope. However euler angle rates and angular velocities are not equivalent as the former are dependant on order of rotation while the latter are a vector expressed in the body frame. For this reason an expression needs to be formulated that connects the two. Since the euler angle rates are expressed in the local frame of that particular rotation sequence, appropriate rotation matrices need to be used to transform them into vectors in the final body fixed frame (B). The order of rotation used here is the intrinsic X-Y'-Z" (roll-pitch-yaw).

$$\begin{pmatrix} {}^B\omega_x \\ {}^B\omega_y \\ {}^B\omega_z \end{pmatrix} = \begin{pmatrix} 0 \\ 0 \\ \dot{\psi} \end{pmatrix} + {}^B R_G \begin{pmatrix} 0 \\ \dot{\theta} \\ 0 \end{pmatrix} + {}^B R_G {}^G R_F \begin{pmatrix} \dot{\phi} \\ 0 \\ 0 \end{pmatrix} \quad (\text{B.1})$$

where ${}^B\omega_x, {}^B\omega_y, {}^B\omega_z$ the angular rates measured by the gyroscope and F, G the local coordinate systems after the first and second rotation respectively. Note that these measurements are corrected for the imperfect orientation of the IMU sensor by transforming with matrix R_{IMU} (see equation (A.6))

$$\begin{pmatrix} {}^B\omega_x \\ {}^B\omega_y \\ {}^B\omega_z \end{pmatrix} = \begin{pmatrix} 1 & 0 & -\sin\theta \\ 0 & \cos\phi & \cos\theta \sin\phi \\ 0 & -\sin\phi & \cos\phi \cos\theta \end{pmatrix} \begin{pmatrix} \dot{\phi} \\ \dot{\theta} \\ \dot{\psi} \end{pmatrix} \quad (\text{B.2})$$

Simply solving equation (B.2) for the euler angle rates yields the expressions that can be used to calculate the roll and yaw rates from gyroscope measurements.

$$\dot{\phi} = ({}^B\omega_y \sin\phi + {}^B\omega_z \cos\phi) \tan\theta + {}^B\omega_x \approx {}^B\omega_x \quad (\text{B.3})$$

$$\dot{\psi} = \frac{{}^B\omega_y \sin\phi + {}^B\omega_z \cos\phi}{\cos\theta} \approx {}^B\omega_y \sin\phi + {}^B\omega_z \cos\phi \quad (\text{B.4})$$

The newly calculated euler angle rate signals can now be numerically integrated to produce the corresponding euler angles. However, a way needs to be found to account for the accumulating integration error. When the whole signal is available, which is true only in offline (post-processing) applications, two methods were tested for approximating euler angles. The first method removes the drift simply through the use of a high-pass filter. All frequency content under 0.05 Hz is filtered. The second method, removes the drift by subtracting the resulting line from a linear regression. Worth noting here that for the yaw angle this will produce good approximations only when the median of the true signal is around zero, which was mostly true since the subjects tried to keep straight heading in order to avoid falling outside the boundaries of the bicycle lane. For the roll angle this assumptions is confidently made since the signal is expected to be centered around zero. The disadvantage of the high-pass filter was that magnitudes of signals are slightly attenuated, while the disadvantage of the linear regression detrending is that a bias can be introduced if the median is not zero.

B.2. ONLINE ESTIMATION METHODS

With no prior knowledge of the resulting drift another method needs to be found to correct the integration output. Fortunately there are existing ways with which two unreliable sources of a signal can be combined in order to produce a more reliable one. For this a secondary source of pseudo measurements is needed.

My first naive implementation was to calculate the roll from the accelerometer data by assuming that gravity is the only force captured in the accelerometer readings. The formulation of the estimators is identical to the equation (A.3). However, this is not ideal for the particular application of single track vehicles since lateral accelerations due to centrifugal forces heavily change the accelerometer measurements.

Sanjurjo et al. [15] used equations B.5 and B.6 as pseudo absolute measurements. Note that B.6 is directly derived from the second equation of B.2. They explain that equation B.5 is more reliable for angles close to zero and equation B.6 is more reliable for larger roll angles, for this reason a weighted sum of the two methods is employed B.7 that follows the weighting function B.8 .

$$\phi_d = \tan^{-1} \left(\frac{\omega_z^B v}{g} \right) \quad (\text{B.5})$$

$$\phi_\omega = \tan^{-1} \left(\frac{\omega_y^B}{\omega_z^B} \right) \quad (\text{B.6})$$

$$\phi_m = W\phi_d + (1 - W)\phi_\omega \quad (\text{B.7})$$

$$W = \exp \left(-\frac{\hat{\phi}^2}{\bar{\phi}^2} \right) \quad (\text{B.8})$$

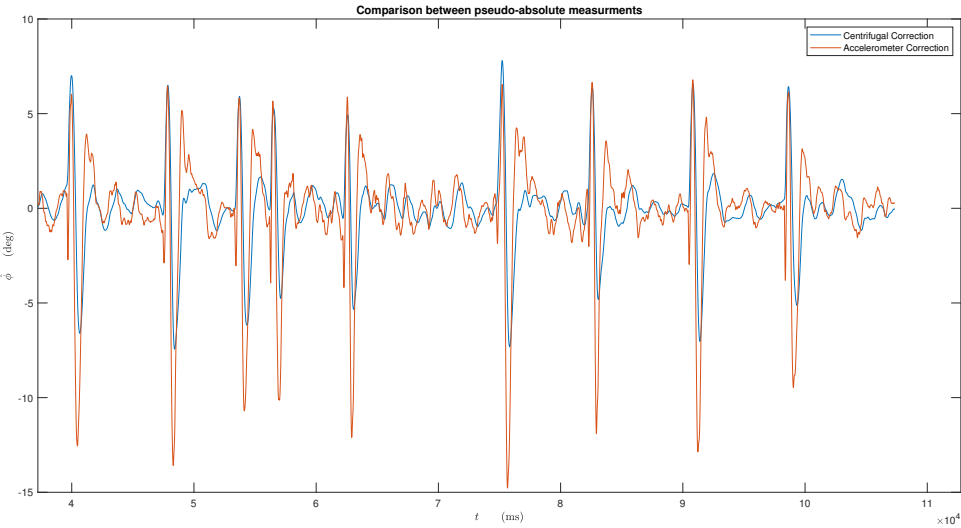
where W is the weighting function, $\hat{\phi}$ is the last available estimation of roll and $\bar{\phi}^2$ is a constant that can be used to adjust the weighting function. Sanjuro et al. used $\bar{\phi}^2 = 0.05$.

For the sensor fusion algorithm both a simple complimentary filter and a Kalman filter were tested. The complementary filter works by combining the desirable low-frequency characteristics of the absolute measurements with the desirable high-frequency characteristics of the euler integration output.

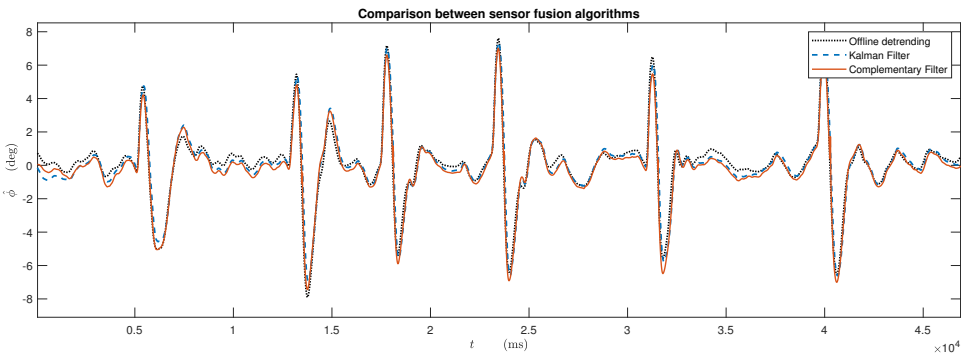
$$\hat{\phi}_k = (1 - \alpha) \cdot (\hat{\phi}_{k-1} + {}^B\omega_{x,k} \cdot dt) + \alpha \cdot \phi_m \quad (\text{B.9})$$

where k is the current iteration of the microcontroller and α is a constant, such that $0 < \alpha < 1$. The larger the α , the more pseudo absolute measurements are 'trusted'. As α goes to zero the estimate is mainly based on the integration output.

On the other hand, Kalman filters are also often used as state estimators when multiple measurement sources need to be combined into a single more reliable one. Often the output of a model is combined with absolute measurements and an estimation of the state is made by dynamically weighting the two sources of information. In this case a simple plant model is created which has $\dot{\phi} \approx {}^B\omega_x$ as input and produces the roll angle of the next time step given the previous one. In order to account for biases in the angular rate sensor an extra



(a) Comparison between pseudo-absolute measurements



(b) Comparison between sensor fusion algorithms

Figure B.1: a) Comparison between pseudo-absolute measurements. Both sources were fused with the integration output via a Kalman filter. The blue line is the result of the measurements used by Sanjurjo et al. [15] while the orange line is the result of the estimation produced using the accelerometer equation (A.3). b) Comparison between sensor fusion algorithms. For reference the output of the offline linear regression detrending is shown as a black dotted line.

state b_x is added to the model. The complete formulation is given by :

$$\begin{bmatrix} \hat{\phi} \\ \hat{b}_x \end{bmatrix}_k^- = \begin{bmatrix} 1 & -dt \\ 0 & 1 \end{bmatrix} \begin{bmatrix} \hat{\phi} \\ \hat{b}_x \end{bmatrix}_{k-1}^+ + \begin{bmatrix} dt \\ 0 \end{bmatrix} {}^B\omega_{x,k-1} \quad (\text{B.10})$$

The results are shown in figure B.1. In figure B.1a it is visible that the naive implementation using the assumption that the accelerometer only registers the gravitational acceleration does not work. However, for the first few seconds after turning on the bike the assumption is correct and a good initial condition estimate can be extracted in order to use as initial condition in the sensor fusion algorithm of choice. As far as the sensor fusion algorithm is concerned the results are shown in figure B.1b. A complimentary filter with $\alpha = 0.0022$ is used, while for the Kalman filter the process covariance matrix and measurement variance were equal to:

$$Q_P = \begin{bmatrix} 9e^{-4} & 0 \\ 0 & 3e^{-4} \end{bmatrix} dt \quad (\text{B.11})$$

$$Q_S = 0.5 \quad (\text{B.12})$$

Additionally the initial covariance matrix was equal to zero which means that the filter at the start "trusts" the model output; the Euler integration output. As a reference the result from the linear regression detrending is

also presented. The graph indicates that both methods successfully approximate the reference result. Furthermore, it is clear that with this general system model, only a slight performance gain (if any) can be gained by using the Kalman filter. Additionally, the implementation of the complimentary filter is far simpler and consequently much less computationally expensive. Had the Kalman filter been implemented on a system where an accurate dynamic model was present, the Kalman filter would – in pretty much all cases – trump the simpler complimentary filter. For this reason the complimentary filter approach was chosen for the on-line implementation of roll estimation in the steer-by-wire bicycle, considering the limiting clock speed of microcontroller Teensy 3.6.

The above pseudo-absolute measurements can only be used to estimate the roll angle. However there is a way to extract an estimation of the yaw relative to the magnetic north by using the magnetometer sensor, which is also part of the IMU. This is similar to how modern smartphones can work as a compass. Similar to how an estimation of the roll angle was made by equating the accelerometer readings with reference position where the gravitational acceleration is completley aligned with the bike's z-axis, the same can be done by equating the magnetometer readings with the reference position of the bike's x axis pointing towards the magnetic north. The magnetometer in this reference position are

$$\mathbf{B}_{ref} = B \begin{pmatrix} \cos \zeta \\ 0 \\ \sin \zeta \end{pmatrix} \quad (B.13)$$

where B is the geomagnetic field strength and ζ is the angle of inclination of the geomagnetic field measured downwards from horizontal. Both values vary over the earth's surface. Detailed geomagnetic field maps are available from the World Data Center for Geomagnetism at <http://wdc.kugi.kyoto-u.ac.jp/igrf/>. Fortunately, both B and ζ cancel out in the final formulation of the estimator.

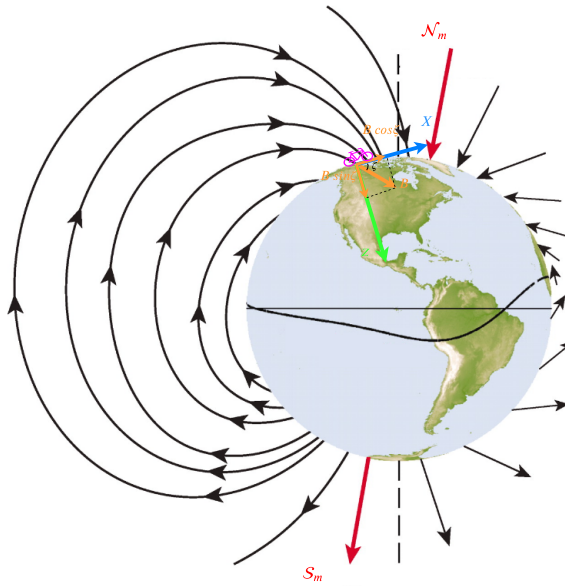


Figure B.2: Magnetic Field vectors in the reference position.

The measured magnetometer readings \mathbf{B}_p after three rotations are described by equations :

$$\mathbf{B}_p = \mathbf{R}_{xyz}(\phi, \theta, \psi) \cdot B \begin{pmatrix} \cos \zeta \\ 0 \\ \sin \zeta \end{pmatrix} + \begin{pmatrix} V_x \\ V_y \\ V_z \end{pmatrix} \quad (B.14)$$

where \mathbf{R}_{xyz} the rotation matrix defined in ??eq:rotmat2) and V_x, V_y, V_z are the components of the Hard-Iron vector, which is a fixed magnetic offset adding to the true magnetometer sensor output. The Hard-Iron offset is the sum of any intrinsic zero field offset within the magnetometer sensor itself plus permanent magnetic

fields within the PCB generated by magnetized ferromagnetic materials. It is quite normal for the Hard-Iron offset to greatly exceed the geomagnetic field. Therefore an accurate Hard-Iron estimation and subtraction are required.

The Hard-Iron offset can be estimated if we consider that the set of all 3d points defined by every magnetometer reading lies in the surface of a sphere with radius B . In the presence of the offset, the center of the sphere would be displaced by the Hard-Iron Vector \mathbf{V} . The components of vector \mathbf{V} can be estimated by fitting the magnetometer measurements to the equation:

$$(\mathbf{B}_p - \mathbf{V})^T (\mathbf{B}_p - \mathbf{V}) = B^2 \quad (\text{B.15})$$

Equation (B.15) was solved with the gradient descend method by minimizing the sum of the squared difference between the right and left hand side of the equation. The resulting Hard-Iron Offset Vector was :

$$\mathbf{V} = \begin{pmatrix} -22.03 & -26.14 & -1.651 \end{pmatrix} \quad [\mu\text{T}] \quad (\text{B.16})$$

In figure B.3 the locus defined by the set of vectors measured by the magnetometer is displayed. It is visible that after the correction the measurements lie on the surface of a sphere with center in the origin and radius approximately equal to 1 a.u.

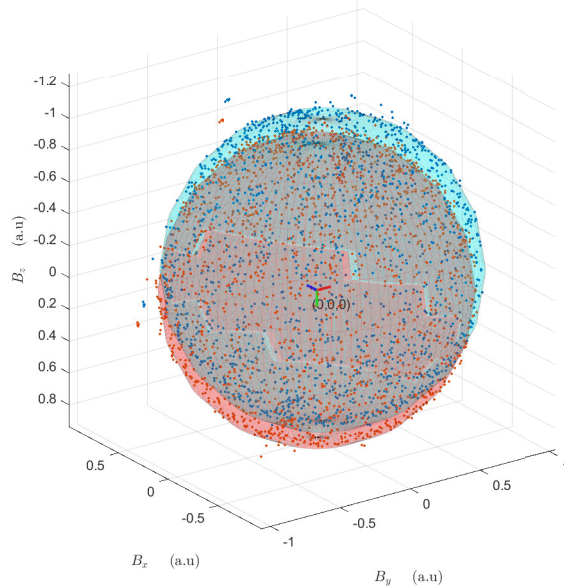


Figure B.3: The blue dots are the locus of the magnetometer readings before correcting for the hard iron offset. The red dots are the locus of the magnetometer readings after correcting for the offset. The magnetometer readings have been normalized so that 1 a.u = 49.0913 μT which is the Magnetic Field Intensity for the approximate location of TU Delft (Latitude 52° 0' 0" N and Longitude: 4° 22' 0" E).

Having estimated \mathbf{V} from equation (B.14) by assuming $\theta \approx 0$ we get :

$$\mathbf{B}_f = \mathbf{B}_p - \mathbf{V} = \mathbf{R}_x(\phi)\mathbf{R}_z(\psi) \cdot \begin{pmatrix} B \cos \zeta \\ 0 \\ B \sin \zeta \end{pmatrix} \quad (\text{B.17})$$

$$\mathbf{R}_x^T(\phi) \begin{pmatrix} B_{fx} \\ B_{fy} \\ B_{fz} \end{pmatrix} = \begin{pmatrix} \cos \psi B \cos \delta \\ -\sin \psi B \cos \delta \\ B \sin \delta \end{pmatrix} \quad (\text{B.18})$$

$$\begin{pmatrix} B_{fx} \\ B_{fy} \cos \phi - B_{fz} \sin \phi \\ B_{fy} \sin \phi + B_{fz} \cos \phi \end{pmatrix} = \begin{pmatrix} \cos \psi B \cos \delta \\ -\sin \psi B \cos \delta \\ B \sin \delta \end{pmatrix} \quad (\text{B.19})$$

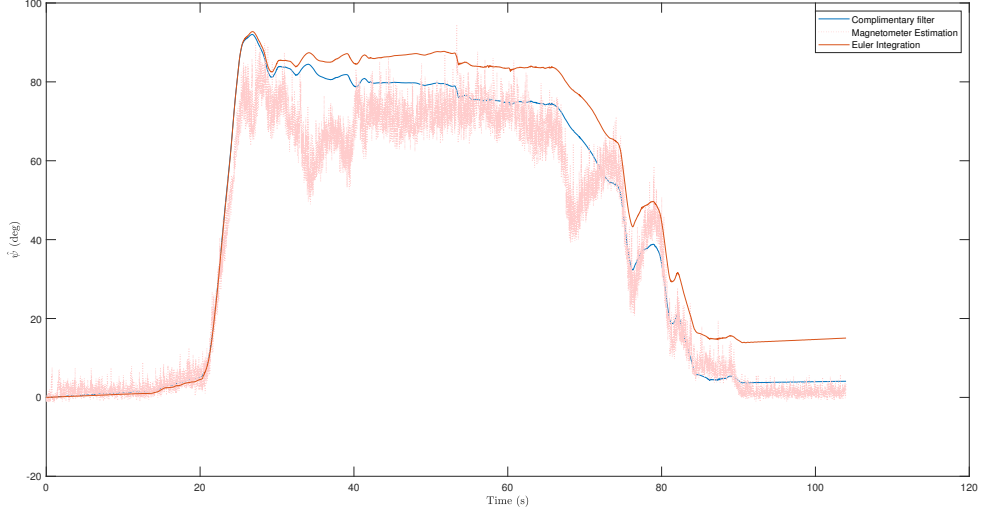


Figure B.4: Comparison of online yaw angle estimation. Red dotted line is the pure estimation from the magnetometer data. Orange line is the drifted euler integration output. Blue line is the result of the complimentary filter sensor fusing the other two signals. For the complimentary filter $a = 0.00027$.

By dividing the y and x component of equation (B.19) we get:

$$\hat{\psi} = \tan^{-1} \left(\frac{B_{fx} \sin \hat{\phi} - B_{fy} \cos \hat{\phi}}{B_{fx}} \right) \quad (\text{B.20})$$

where $\hat{\phi}$ is the estimate of roll angle obtained from the aforementioned methods. Equation (B.20) can now be used as a source of pseudo-absolute measurements for the sensor fusion algorithm of choice. Regarding signal fusion the same things apply as in the roll angle estimation case. Finally since we want the yaw angle relative to the starting position and not relative to the magnetic north the value of the first yaw estimation is subtracted from all subsequent computations.

C

ESTIMATION OF RIDER TORQUE

Given the steer rate ($\dot{\delta}$) and acceleration ($\ddot{\delta}$), moment of inertia (I_H), motor damping (b_m) and the torque applied by the handlebar motor (T_{PDH}) the equation of motion of the upper handlebar assembly can be formed (see Fig. C.1) and solved for the unknown rider input torque (T_H).

$$T_H = \ddot{\delta} I_H + \dot{\delta} b_m - T_{PDH} \quad (\text{C.1})$$

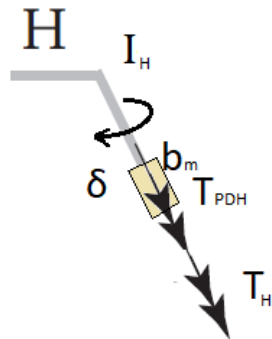


Figure C.1: Free body diagram of the upper handlebar assembly.

C.1. STEER RATE AND ACCELERATION

Since only the steering angle is directly measurable, a way needs to be found that produces accurate estimations of steer rate and steer acceleration. Simple numerical differencing techniques proved ineffective as noise effects were magnified resulting in corrupted second derivatives, even after filtering the original signal to a cutoff frequency of 10 Hz.

To combat this problem a piecewise cubic interpolation technique using the cubic spline function was used. The principle of this method is simple. Third order polynomials are fitted between the datapoints. This results in a signal that is identical to the original but instead of discrete points, it is represented by the union of polynomial functions. After this point the steer rate and acceleration can be easily obtained by taking the derivatives of the polynomials. the result of the method is seen in figure C.2.

C.2. STEERING SHAFT MOMENT OF INERTIA AND VISCOUS FRICITION

In order to make estimation of applied rider torque, the damping coefficient and the inertia of the steering shaft needs to be determined. There are multiple ways to measure inertia of complex geometries. Here an

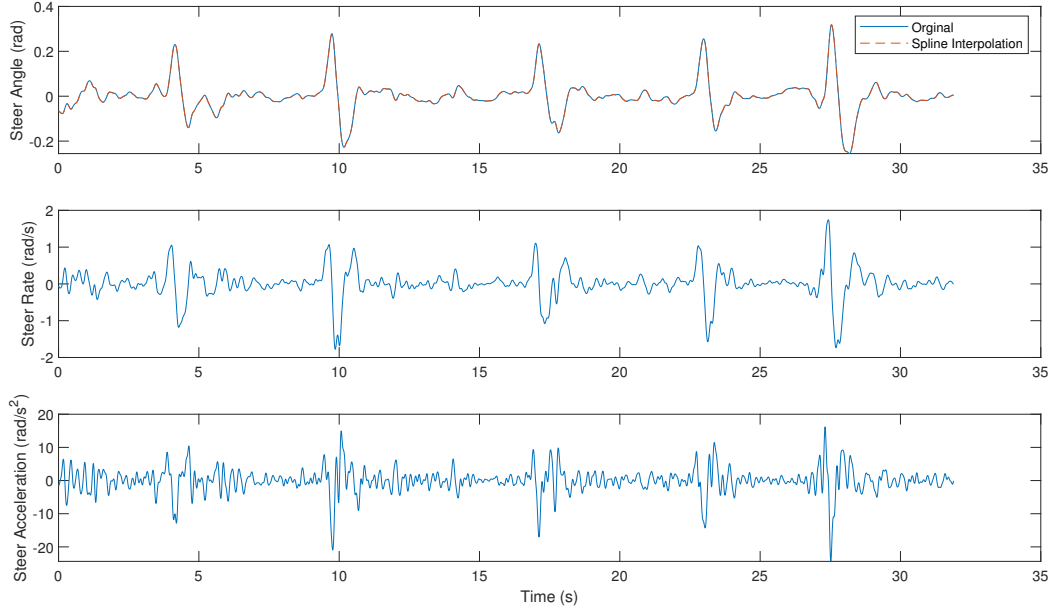


Figure C.2: Steering angle signal with its derivates produced by the piecewise cubic spline interpolation method.

estimation through a simple experimental setup is chosen.

By connecting the steering shaft with two extension springs (see Fig.C.3) and measuring the oscillations of the steering angle δ , a mechanical system is created where it has to obey equation C.2.

$$I_H \ddot{\delta}(t) + b_m \dot{\delta}(t) + 2K\alpha^2 \delta(t) = 0 \quad (\text{C.2})$$

where K the spring elastic constant and α the moment arm shown in figure C.3.

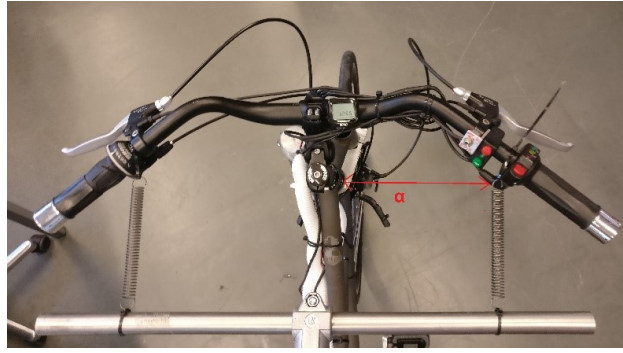


Figure C.3: Spring-handlebar assembly where α is the moment arm.

The springs ($K = 555 \text{ N/m}$ and slack length of 0.03 m) are attached to the handlebar and the system is perturbed. The measured steering angle signal from one of the perturbation tests is shown in figure C.4. The steering rate and acceleration signals are derived by the methods described in section C.1. Equation C.2 is then applied to all discrete time steps and so the system of equations C.3 is created.

$$\begin{bmatrix} \ddot{\delta}_1 & \dot{\delta}_1 \\ \ddot{\delta}_2 & \dot{\delta}_2 \\ \vdots & \vdots \\ \ddot{\delta}_N & \dot{\delta}_N \end{bmatrix} \begin{bmatrix} I_H \\ b_m \end{bmatrix} = -2K\alpha^2 \begin{bmatrix} \delta_1 \\ \vdots \\ \delta_N \end{bmatrix} \quad (\text{C.3})$$

where N the length of the recorded signal.

Since equation C.3 is linear in the parameters, the solution of the regression problem can be approximated by the use of the least squares method.

$$\begin{bmatrix} I_H \\ b_m \end{bmatrix} = -2K\alpha^2 \left(\begin{bmatrix} \ddot{\delta}_1 & \dot{\delta}_1 \\ \ddot{\delta}_2 & \dot{\delta}_2 \\ \vdots & \vdots \\ \ddot{\delta}_N & \dot{\delta}_N \end{bmatrix}^T \begin{bmatrix} \ddot{\delta}_1 & \dot{\delta}_1 \\ \ddot{\delta}_2 & \dot{\delta}_2 \\ \vdots & \vdots \\ \ddot{\delta}_N & \dot{\delta}_N \end{bmatrix} \right)^{-1} \begin{bmatrix} \ddot{\delta}_1 & \dot{\delta}_1 \\ \ddot{\delta}_2 & \dot{\delta}_2 \\ \vdots & \vdots \\ \ddot{\delta}_N & \dot{\delta}_N \end{bmatrix}^T \begin{bmatrix} \delta_1 \\ \dots \\ \delta_N \end{bmatrix} \quad (\text{C.4})$$

The system is perturbed 15 times so 15 sets of inertia and damping ratios are computed. The mean of the these was taken and resulted in $I_H = 0.0960 \text{ kg m}^2$ and $b_m = 0.2663 \text{ N s}^{-1}$

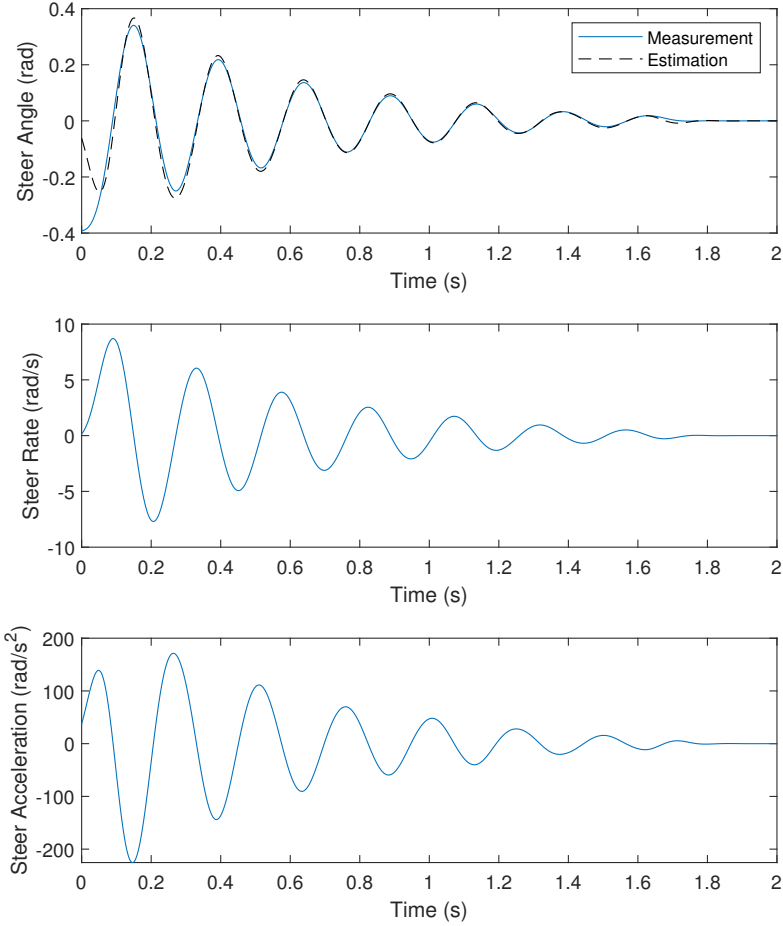


Figure C.4: Result of the first of fifteen oscillations. Blue lines indicate the measured signals while the black dotted line is the output of the model given the values of inertia and damping estimated with the least squares method.

C.3. MOTOR TORQUE INPUT VALIDATION

C.3.1. DESIGN OF TORQUE SENSOR

In order to validate that the torque exerted by the handlebar motor results in equivalent input rider torque a torque sensor is designed and attached to the steering shaft. The most common torque sensor measurement principle uses bonded strain gauge technology, where the strain gauges are bonded to a suitably designed shaft.

In the torsion of a cylindrical shaft the strain is measured by the angle of twist or angular deflection. Unfortunately stain gauges can only detect compressive and tensile strain. The strain gauges are placed with such an orientation that the shearing stress is replaced by its equivalent principal stresses. The angle and the magnitude of the principal stresses are calculated by the use of the Mohr Circle. In this case the principal tension and compressive stresses are of the same magnitude as the shearing stress and are active at an angle of 45 degrees since it is considered that no external compressive or tension force is present.

In order to design a proper cylindrical shaft for the torque sensor the diameter of the shaft is chosen such that the strain measured in the strain gauges is within the detectable range ($\epsilon_{min} = 10^{-5}$, $\epsilon_{max} = 6 \cdot 10^{-4}$). For this application, a hollow cylindrical shaft made of aluminum (AL7075 – O) is used so the unknowns are the inner and outer diameters. The strain is given in relation to the stress by Hooke's law for isotropic materials by equation (C.5). The shearing stress is in turn given by equation (C.6).

$$\epsilon = \frac{\sigma \cdot (1 + \nu)}{E} \quad (\text{C.5})$$

where ν the Poisson's ratio and E the Young's Modulus (Pa)

$$\tau = \frac{T \cdot r}{J} \quad (\text{C.6})$$

where J is the polar moment of inertia (m^4), r the distance from center to stressed surface in the given position (mm), T the twisting moment (Nm). The polar moment of inertia of a circular hollow shaft can be expressed as

$$J = \frac{\pi \cdot (D^4 - d^4)}{32} \quad (\text{C.7})$$

where d is shaft inside diameter (mm) and D is the shaft outside diameter (mm).

By inputting the above equations into a MATLAB script figure C.5 was produced. The figure was created for a fixed inner diameter of 12mm, due to limitations in the machining process. It is evident that the lower the width of the shaft the higher detection of the low level torques. For this reason a width of 2 mm was chosen. This still means that torques below 0.2Nm are not detectable. However the purpose of the torque sensor is not to provide accurate online measurements but to validate the input torques from the handlebar motor. The design of the resulting part is shown in C.6.

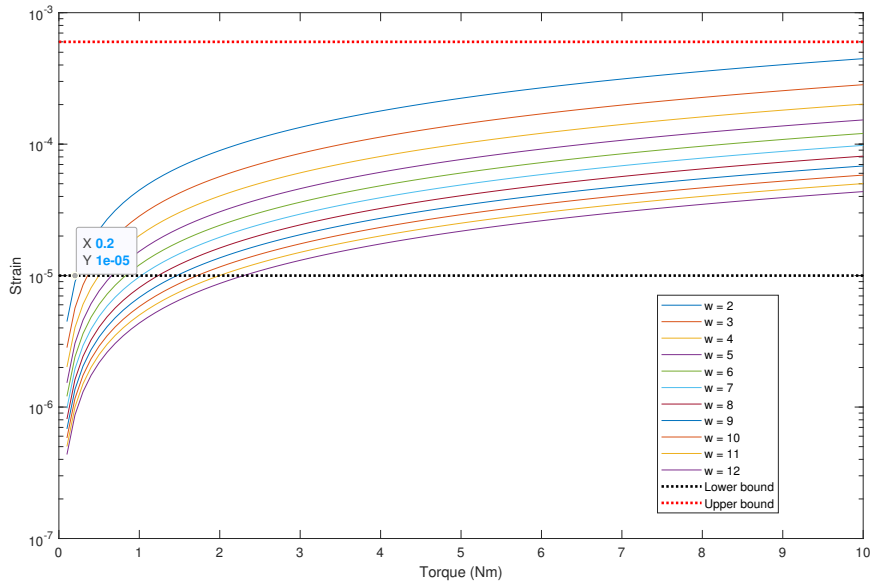


Figure C.5: Principal tensile strain in the 45 degree angle for various shaft widths (w).

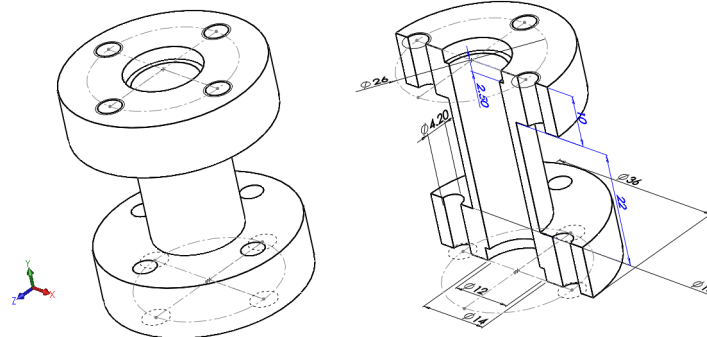


Figure C.6: Schematic of the hollow shaft.

Because it is not an ideal hollow cylinder, the shearing stress calculated analytically from the above equations needs to be validated. A static load simulation in SolidWorks is done to see how much different is the shearing stress on the external surface. As it turns out the simulation showed a shearing stress similar to the one calculated by the equations. In C.7 the simulation results for a loading of 10Nm is shown. For comparison the resulting shearing stress calculated analytically is $10.0874 \cdot 10^6 N/m^2$. For proper measurements of strain the gauge placement should gravitate towards the middle to avoid the spikes of shearing stress near the intersections between the main shaft and the cylindrical heads (see fig. C.7)

C.3.2. RESULTS

In order to validate that the commanded torque in the handlebar motor is the same as the one actually applied in the handlebar, a trial identification run was conducted to simulate steer torque levels of the experiments. The signal of the input motor torque is compared with the output of the custom made torque sensor. The results are shown in figure C.8. The mismatch of the two signals for values lower than 0.5Nm is attributed to the fact that the sensor's strain gauges cannot accurately measure the strain in the material to produce reliable ouput as determined analytically beforehand. Also during the measurements a slight bias of the sensor was noted when $0 < \delta < \pi/2$. Despite the aforementioned, the resulting Variance Accounted For (VAF) was

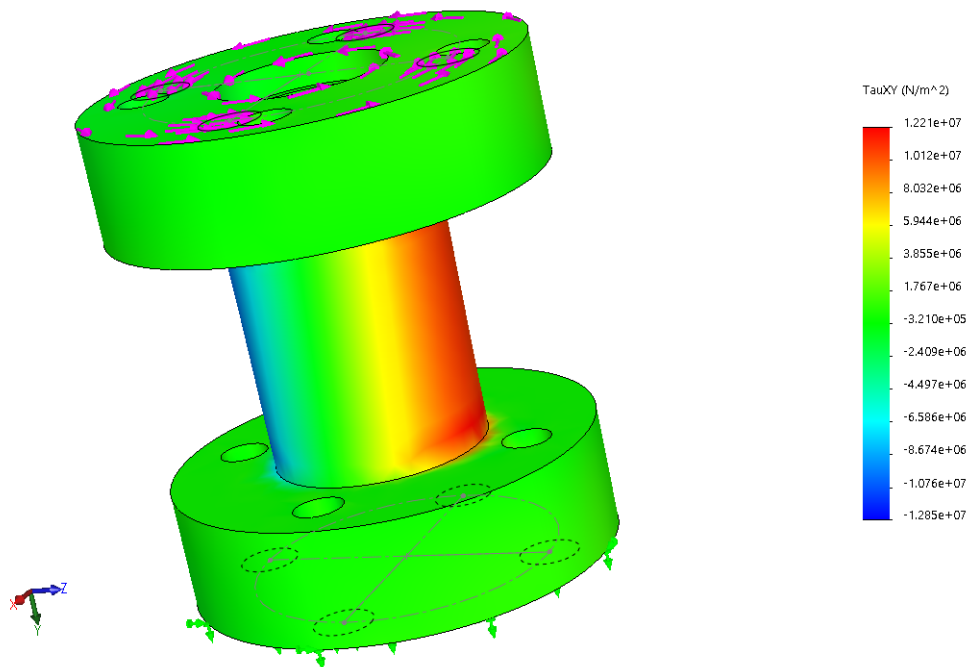


Figure C.7: Shearing stress for $10Nm$ loading in the axial direction.

equal to 90.77% and was deemed that the motor command torque is indeed what is being applied in the steering shaft so in all subsequent calculation it was taken as ground truth.

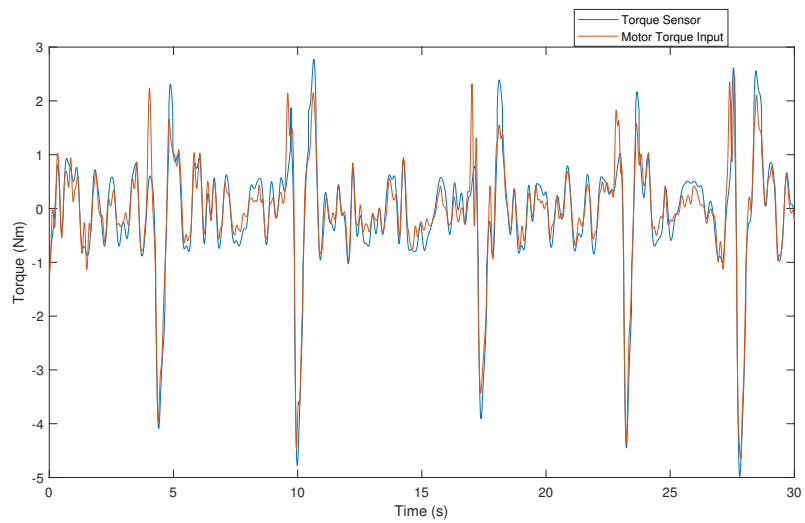


Figure C.8: Measurement of torque sensor compared to the commanded torque of the handlebar motor.

BIBLIOGRAPHY

- [1] Michael Barnett-Cowan. Vestibular perception is slow: a review. *Multisensory research*, 26(4):387–403, 2013.
- [2] Laura Marchal Crespo and David J Reinkensmeyer. Haptic guidance can enhance motor learning of a steering task. *Journal of motor behavior*, 40(6):545–557, 2008.
- [3] Erwin De Vlugt, Alfred C Schouten, and Frans CT Van Der Helm. Adaptation of reflexive feedback during arm posture to different environments. *Biological cybernetics*, 87(1):10–26, 2002.
- [4] Georgios Dialynas, Christos Christoforidis, Riender Happee, and AL Schwab. The effect of haptic feedback in the balance task of bicycling. *Symposium on the Dynamics and Control of Single Track Vehicles*.
- [5] Georgios Dialynas, Riender Happee, and AL Schwab. Design and implementation of a steer-by-wire bicycle. In *Proceedings of the 7th Annual International Cycling Safety Conference*, 2018. URL <https://www.researchgate.net/publication/328808185>.
- [6] Riender Happee, Erwin De Vlugt, and Alfred C Schouten. Posture maintenance of the human upper extremity; identification of intrinsic and reflex based contributions. *SAE International Journal of Passenger Cars-Mechanical Systems*, 1(2008-01-1888):1125–1135, 2008.
- [7] Ryouhei Hayama, Sadahiro Kawahara, Shirou Nakano, and Hiromitsu Kumamoto. Resistance torque control for steer-by-wire system to improve human-machine interface. *Vehicle system dynamics*, 48(9):1065–1075, 2010.
- [8] JDG Kooijman, Jacob Philippus Meijaard, Jim M Papadopoulos, Andy Ruina, and AL Schwab. A bicycle can be self-stable without gyroscopic or caster effects. *Science*, 332(6027):339–342, 2011.
- [9] Y Marumo and M Nagai. Steering control of motorcycles using steer-by-wire system. *Vehicle System Dynamics*, 45(5):445–458, 2007.
- [10] Yoshitaka Marumo and Nozomi Katagiri. Control effects of steer-by-wire system for motorcycles on lane-keeping performance. *Vehicle System Dynamics*, 49(8):1283–1298, 2011.
- [11] Jaap P Meijaard, Jim M Papadopoulos, Andy Ruina, and Arend L Schwab. Linearized dynamics equations for the balance and steer of a bicycle: a benchmark and review. *Proceedings of the Royal society A: mathematical, physical and engineering sciences*, 463(2084):1955–1982, 2007.
- [12] RC Miall, D Jo Weir, Daniel M Wolpert, and JF Stein. Is the cerebellum a smith predictor? *Journal of motor behavior*, 25(3):203–216, 1993.
- [13] Jason K Moore, JDG Kooijman, AL Schwab, and Mont Hubbard. Rider motion identification during normal bicycling by means of principal component analysis. *Multibody System Dynamics*, 25(2):225–244, 2011.
- [14] Jason Keith Moore. *Human control of a bicycle*. University of California, Davis Davis, CA, 2012.
- [15] Emilio Sanjurjo, Miguel A Naya, Javier Cuadrado, and Arend L Schwab. Roll angle estimator based on angular rate measurements for bicycles. *Vehicle System Dynamics*, pages 1–15, 2018.
- [16] Emilio Sanjurjo, Miguel A Naya, Javier Cuadrado, and Arend L Schwab. Roll angle estimator based on angular rate measurements for bicycles. *Vehicle System Dynamics*, 57(11):1705–1719, 2019.
- [17] OJM Smith. Closed control of loops with dead time. *Chemical Engineering Progress*, 53:217–219, 1957.

- [18] Frans CT Van der Helm, Alfred C Schouten, Erwin de Vlugt, and Guido G Brouwn. Identification of intrinsic and reflexive components of human arm dynamics during postural control. *Journal of neuroscience methods*, 119(1):1–14, 2002.
- [19] Herman van der Kooij, Ron Jacobs, Bart Koopman, and Frans van der Helm. An adaptive model of sensory integration in a dynamic environment applied to human stance control. *Biological cybernetics*, 84(2):103–115, 2001.
- [20] Sarah Catherine Walpole, David Prieto-Merino, Phil Edwards, John Cleland, Gretchen Stevens, and Ian Roberts. The weight of nations: an estimation of adult human biomass. *BMC public health*, 12(1):439, 2012.
- [21] David H Weir. A manual control view of motorcycle handling. Technical report, 1973.